

PEPSI Investigation, Retrieval, and Atlas of Numerous Giant Atmospheres (PIRANGA). II. Phase-Resolved Cross-Correlation Transmission Spectroscopy of KELT-20b

CALDER LENHART ¹, MARSHALL C. JOHNSON ¹, JI WANG (王吉) ¹, ANUSHA PAI ASNODKAR ¹, SYDNEY PETZ ¹,
ALISON DUCK ¹, KLAUS G. STRASSMEIER ², AND ILYA ILYIN ²

¹Department of Astronomy, The Ohio State University, 4055 McPherson Laboratory, 140 West 18th Avenue, Columbus, OH 43210, USA

²Leibniz-Institut für Astrophysik Potsdam, An der Sternwarte 16, D-14482 Potsdam, Germany

ABSTRACT

KELT-20b is a well-studied exoplanet within the highly observable ultra hot Jupiter (UHJ) regime, yet its multidimensional atmospheric structure remains largely unconstrained. Recent advances in instrumentation and increased general circulation model (GCM) complexity have enabled observers to resolve the imprints of more intricate physical mechanisms in time-resolved data. We performed high-resolution cross-correlation transmission spectroscopy (HRCCTS) on a single transit time series of KELT-20b, observed with PEPSI on the LBT. We detect Fe I (11.9σ) and Fe II (23.7σ) and tentatively detect Na I (3.4σ) and Cr I (3.3σ) upon combining nineteen in-transit exposures. The full-transit velocity offsets of the strongest absorbers are $\Delta V_{\text{Fe I}} = -1.0 \pm 0.7 \text{ km s}^{-1}$ and $\Delta V_{\text{Fe II}} = 0.0 \pm 0.5 \text{ km s}^{-1}$. These results are discrepant with other HRCCTS studies of KELT-20b, but these studies are largely inconsistent with each other due to multiple possible factors, including self-inconsistent treatment of systemic velocity. In response, we establish a stringent set of detection criteria to promote reproducibility in future works. We present phase-resolved absorption traces of species with high detection significance. Fe I and Fe II's absorption traces are both redshifted at ingress, cross to a blueshift after mid-transit, then settle at a net blueshift at egress; concurrently, SNR increases with phase. This behavior is consistent with absorption traces post-processed from an active magnetic drag GCM for another UHJ. However, the net blueshift during transit could also result from limb asymmetry drivers and/or longitudinally variable wind structure. This ambiguity motivates future theoretical work on KELT-20b.

Keywords: Doppler shift, Exoplanet atmospheric dynamics, Exoplanet atmospheric structure, High resolution spectroscopy, Hot Jupiters, Transmission spectroscopy

1. INTRODUCTION

Ultra hot Jupiters (UHJs) are an exceptional subclass of exoplanets that are highly irradiated, inflated, and expected to be tidally locked. They have equilibrium temperatures $T_{eq} \geq 2150 \text{ K}$ (M. Stangret et al. 2022), making them particularly amenable to atmospheric characterization.

Transmission spectroscopy is the primary tool used to probe low-pressure ($\sim 10^{-2} - 10^{-6} \text{ bar}$) UHJ upper atmospheres at their terminator. The advent of ground-based spectrographs with resolving power $\frac{\lambda}{\Delta\lambda} = \mathcal{R} \sim 10^5$ on 8-10m telescopes enabled high-resolution cross-correlation transmission spectroscopy (HRCCTS). I. A. G. Snellen et al. (2010) introduced the cross-

correlation technique for exoplanet transmission spectroscopy. Instead of analyzing transmission spectra line-by-line, a generated template spectrum and the observed spectrum were cross-correlated, enhancing the atmospheric absorption signal for species with many lines in the bandpass. The cross-correlation functions (CCFs) of each usable in-transit exposure were stacked together to increase signal strength. Absorption lines, and thus CCFs Doppler shifted with respect to the planetary rest frame, quantified the atmospheric dynamics. Work by D. Ehrenreich et al. (2020) on WASP-76b presented CCFs of each exposure with respect to time, introducing phase-resolved HRCCTS and enabling observational probes of multidimensional wind structures (E. Miller-Ricci Kempton & E. Rauscher 2012).

Phase-resolved HRCCTS analyses can bin a limited number of in-transit exposures together to retain time

resolution, yet maintain a significant signal during transit. We can fit Gaussian profiles to each phase-resolved CCF and record their centroids, then trace their velocities during transit. Theoretical models have long presented simulated phase-resolved velocities (J. P. Wardenier et al. 2021, 2023; A. B. Savel et al. 2022, 2023, 2024; H. Beltz et al. 2021, 2022, 2023), so connecting the many models with observation allows mapping to a range of dynamical, radiative, and chemical mechanisms. KELT-20 is rapidly rotating, so stellar spectral lines are broadened to the point that only an upper limit is established on the planetary mass, which inhibits modeling. Thus, no model specific to KELT-20b has been published yet; we aim to motivate its development with this work.

Phase-resolved Doppler-shifted cross-correlation signals of individual species templates and high resolution transmission spectra are one of the most promising tools in exoplanetary characterization, granting an unprecedented interface between exoplanet atmosphere theory and observation. However, in its current state, the exoplanet HRCCTS subfield is replete with inconsistent results (see Section 4.2). To promote consistency between our work and future studies of KELT-20b in identifying and validating cross-correlation signals, we explicitly outline our detection criteria. Phase-resolved velocity offsets of UHJs have been analyzed for WASP-33b (P. W. Cauley et al. 2021), WASP-76b (D. Ehrenreich et al. 2020; A. Y. Kesseli et al. 2022), WASP-121b (J. P. Wardenier et al. 2024), WASP-189b (B. Prinoth et al. 2023), KELT-9b (P. W. Cauley et al. 2019; L. Pino et al. 2022), and KELT-20b (H. J. Hoeijmakers et al. 2020; M. Rainer et al. 2021).

This work seeks to reproduce previous detections of atomic species in the atmosphere of KELT-20b, report previously undetected species, and phase-resolve Doppler-shifted signals at an increased time resolution. We intend to complement simulated wind velocity versus orbital phase plots, e.g., A. B. Savel et al. (2022, 2023); J. P. Wardenier et al. (2023), with our observational data. We remove the Doppler shadow from the phase-resolved CCFs to maintain signal clarity throughout transit. We diagnose drivers of observed phase asymmetries by relating a set of phase-binned CCFs of each species to several model predictions.

This paper is organized as follows: in Section 2, we describe the observation. In Section 3, we describe model spectra generation and data processing of observed spectra, data cleaning steps, cross-correlation of the model and data, Doppler shadow removal, and phase-binning procedure. We also detail our detection criteria. In Section 4, we compile full-transit detections from all previous high-resolution transmission spectroscopy and HRC-

CTS papers on KELT-20b alongside our own. We also present phase-resolved velocity offsets, compare the absorption traces to theory, and search for behavior that is consistent with limb asymmetry drivers. We also explore nondetections and aliasing and discuss the impact of discrepancies in methodology on results across the literature for KELT-20b. In Section 5, we review our results and motivate future observation and modeling of KELT-20b.

2. OBSERVATION

We observed a single transit event with the Potsdam Echelle Polarimetric and Spectroscopic Instrument (PEPSI) (K. Strassmeier et al. 2015) on the Large Binocular Telescope (LBT), which has a resolving power $\mathcal{R} = 130000$. We utilized the PEPSI CD III+V bandpass, with a blue arm of 4800–5441Å and red arm of 6278–7419Å. To maximize signal recovery without sacrificing line measurement precision due to Doppler smearing, we took 600 s exposures (see Section B.2 for further discussion). The blue arm spectrograph signal-to-noise ratio S/N_{blue} ranged from 272–330 during the observation, and S/N_{red} ranged from 246–319, as shown in Figure 1. We list the remaining key observation parameters in Table 1. We reduced this observation using the Spectroscopic Data Systems (SDS) Pipeline, as detailed by I. V. Ilyin (2000); K. G. Strassmeier et al. (2018). Limited analysis of these data were done by A. Pai Asnodkar et al. (2022) and M. C. Johnson et al. (2023), but this work treats them comprehensively.

3. METHODOLOGY

3.1. Model spectra

We generate model transmission spectra in 0.01 Å steps from 3850–7500 Å with the `petitRADTRANS` package (P. Mollière et al. 2019). We use physical and orbital parameters from one of the discovery papers (M. B. Lund et al. 2017) and ephemerides by Duck et al. (in prep). The updated transit timings are part of a larger effort—to be presented by Duck et al. (in prep)—to update ephemerides with `EXOFASTv2` (J. D. Eastman et al. 2019) fits to *TESS* photometry. We also use pressure-temperature (P-T) profile parameters from M. C. Johnson et al. (2023), and systemic velocity derived by S. Petz et al. (2023); each are listed in Table 2. We reuse the systemic velocity found by S. Petz et al. (2023) since it utilized three PEPSI observations: two emission datasets and one transmission dataset, including ours. We select a P-T profile given by Equation 29 of T. Guillot (2010) with best-fit parameters $\gamma = 30$ and $\kappa_{\text{IR}} = 0.04$ as obtained in a grid search in M. C. Johnson et al. (2023). While these parameters were derived us-

Table 1. Parameters of the single transit observation. N_{spec} is the amount of exposures, or spectra, collected in the observation, while $N_{\text{spec, in-transit}}$ are those taken between T_{14} . T_{exp} is the time of each exposure. S/N_{blue} and S/N_{red} are the mean of the 95th quantile per-pixel S/Ns in the blue and red arms, respectively, during transit.

Parameter	Value
Date (UT)	2019 May 4
Telescope	LBT
Instrument	PEPSI
N_{spec}	23
$N_{\text{spec, in-transit}}$	19
T_{exp} (s)	600
Airmass Range	[1.00, 2.01]
Phase Range ($^{\circ}$)	[-8.28, 12.24]
S/N_{blue}	288
S/N_{red}	308

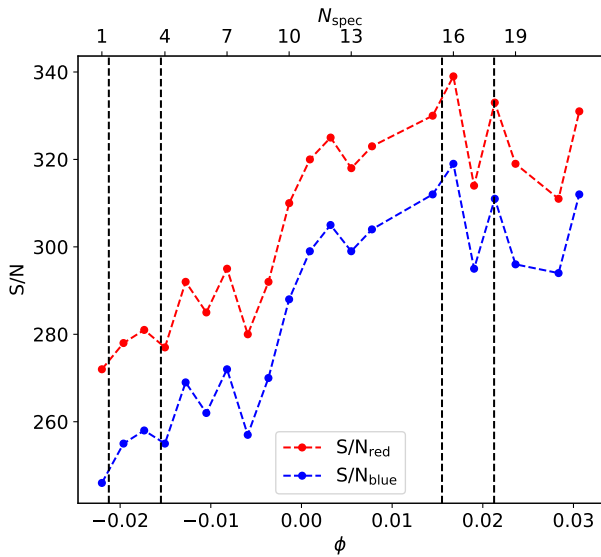


Figure 1. S/N versus the corresponding orbital phase at the center of the each exposure. The red and blue arms of PEPSI are color-coded. The vertical lines correspond to T_1 , T_2 , T_3 , T_4 , in order. There is a marked increase in S/N with phase, which impacts our interpretation of time-resolved CCFs, further discussed in Section 4.3.

ing emission spectra, transmission spectra are less sensitive to detailed vertical temperature structures (I. A. G. Snellen et al. 2010; A. Y. Kesseli et al. 2020). Since our analysis concerns the atmospheric dynamics instead of chemistry, we deem the same profile sufficient for this analysis.

We calculate volume mixing ratios (VMRs) for each species using the `PyFastChem` equilibrium chemistry model (J. W. Stock et al. 2018a, 2022; D. Kitzmann et al. 2023), assuming solar abundances (M. Asplund et al. 2021) and the aforementioned P-T profile. In our model, we assume that below a certain pressure level, the atmospheric mixing timescale becomes shorter than the chemical reaction timescale. This quench point sets the pressure level at which chemical abundances are frozen-in and transported upward without further reaction. We assume a quench point of 1 bar, in line with S. Petz et al. (2023); M. C. Johnson et al. (2023), thus approximating each species’ VMR as constant. Since we are probing the upper atmosphere, the non-local thermodynamic equilibrium condition necessitates radiative transfer simulation beyond the scope of this work. We set the VMRs of ionized species equal to those of their neutral counterparts to simplify our analysis. We again note that our VMR limits are approximate as they are dependent on a simplified P-T profile previously constrained for an emission spectrum and a 1 bar quench pressure.

Atomic and molecular opacities were sourced from the `petitRADTRANS` database³, with missing entries supplemented from the DACE Opacity Database⁴ and converted to `petitRADTRANS`-compatible format (P. Mollière, private communication). `petitRADTRANS` sources its atomic opacities from the Kurucz line list, and we ensured the DACE opacities—Na I and Co I—came from the same line list⁵. We used several DACE molecular opacity datasets, including the C. A. Bowesman et al. (2021) line list for AlO, S. N. Yurchenko et al. (2016) line list for CaO, and T. Rivlin et al. (2015) line list for NaH.

We calculated an observability score for each neutral atom using methodology described in Appendix B.1. The results are shown in Figure 2. Mg, Ca, Ti, Cr, Fe, and Ni are all deemed observable in our study, so we expect their CCF to exceed the tentative detection threshold. We will further analyze any nondetections of species deemed observable, and scrutinize any detections

³ https://petitradtrans.readthedocs.io/en/2.7.7/content/available_opacities.html

⁴ <https://dace.unige.ch/opacityDatabase/>

⁵ <http://kurucz.harvard.edu/>

Table 2. A summary of the stellar, planetary, and updated ephemerides used in our analysis. Sources: (a) M. B. Lund et al. (2017); (b) M. C. Johnson et al. (2023); (c) S. Petz et al. (2023); (d) Duck et al. (in prep).

Parameter	Symbol (Unit)	Value	Source
Stellar Parameters			
Stellar radius	R_* (R_\odot)	1.565	(a)
Stellar mass	M_* (M_\odot)	1.76	(a)
Stellar effective temperature	T_{eff} (K)	8720	(a)
Metallicity	[Fe/H]	-0.29	(a)
Stellar surface gravity	$\log g_*$	$4.290^{+0.017}_{-0.020}$	(a)
Stellar rotational velocity	$v \sin i_*$ (km s^{-1})	117.4 ± 2.9	(a)
Planetary Parameters			
Planet radius	R_P (R_J)	1.741	(a)
Planet mass	M_P (M_J)	< 3.382	(a)
Equilibrium temperature	T_{eq} (K)	2262	(a)
Planetary radial velocity semi-amplitude	$K_{P,\text{expected}}$ (km s^{-1})	169.0 ± 6.1	(a)
Projected equatorial rotational velocity	$v \sin i_P$ (km s^{-1})	2.5	(a)
Orbital inclination	i ($^\circ$)	$86.12^{+0.28}_{-0.27}$	(a)
Semimajor axis	a (AU)	0.0542	(a)
Eccentricity	e	0	(a)
Infrared opacity	κ_{IR}	0.04	(b)
Ratio of optical to infrared opacities	γ	30	(b)
Reference pressure	P_0 (bar)	1	(b)
Atmospheric abundance of H	X_{H_2}	0.7496	(b)
Atmospheric abundance of He	X_{He}	0.2504	(b)
Volume mixing ratio of H^-	VMR (H^-)	1×10^{-9}	(b)
Updated Ephemerides			
Systemic velocity	v_{sys} (km s^{-1})	-22.78 ± 0.11	(c)
Orbital period	P (d)	$3.47410151 \pm 0.00000012$	(d)
Epoch of mid-transit	T_0 (BJD _{TDB})	$2459757.811176 \pm 0.000019$	(d)
Transit duration	T_{14} (d)	$0.147565^{+0.000091}_{-0.000092}$	(d)
Ingress/egress duration	τ (d)	0.02007 ± 0.00011	(d)

of species with low observability using methods further discussed in Section 3.5. One caveat to this methodology is that it favors many lines over a few strong lines, so a species may have little to no observability yet remain detectable, and vice versa. However, a species that exhibits only a few strong lines may be more susceptible to aliasing with a species that has many lines; thus, a low observability score should prompt caution during detection assessment.

3.2. Data preparation

The following pipeline is nearly identical to M. C. Johnson et al. (2023) and S. Petz et al. (2023). Our systematics correction method employs both the `molecfits` package (A. Smette et al. 2015; W. Kausch et al. 2015) and a modified version of the `PySysRem`⁶ package that

accepts PEPSI data. As determined in M. C. Johnson et al. (2023), applying both methods yields increased significance of retrieved signals than either alone.

`molecfits` fits a model of the telluric spectrum to the data, finds the best-fit model, then removes it. We apply `molecfits` to the red arm spectra only, as the blue arm is absent of significant tellurics (A. Smette et al. 2015). We split the red arm spectra into a region with $> 1\%$ line depth in adjacent lines (telluric region) and a region with $\leq 1\%$ line depth in adjacent lines (non-telluric region). We import the flux values for each spectrum, then regrid the fluxes to common wavelength values for each spectrum. Next, we flatten both arms of the time-series spectra by subtracting off the median flux from each, yielding residual spectra with stellar lines and time-invariant telluric lines removed. Finally, we apply SYSREM to the residual spectra. The SYSREM detrending algorithm (O. Tamuz et al. 2005)

⁶ <https://github.com/stephdouglas/PySysRem>

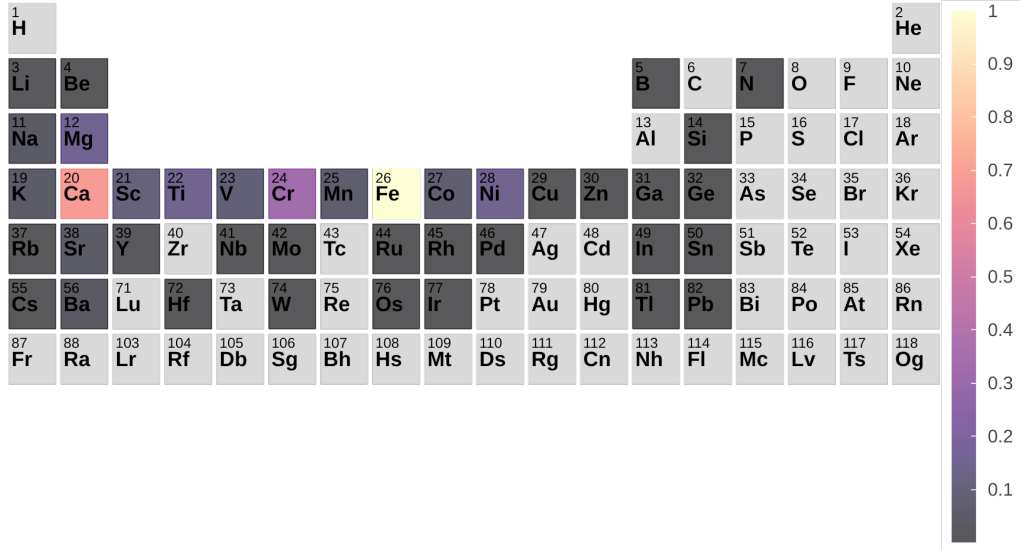


Figure 2. Observability score of each neutral species considered in this study. Colored elements are more likely to be detected since their absorption lines are covered by the PEPSI bandpass ranges we use. Dark cells have fewer and/or shallower lines. Light gray cells were skipped because they don’t have significant lines in the PEPSI bandpass or did not have available opacities. Species with observability score of ~ 0.2 or greater have been detected in at least one study, except for Ni I.

Table 3. Optimal SYSREM iterations (N_{Sys}) for systematics reduction for each species meeting the tentative detection. We separate the telluric and non-telluric contaminated wavelength regions, finding the best N_{Sys} for each. The telluric regions are as follows: $6278 \text{ \AA} < \lambda \leq 6328 \text{ \AA}$, $6459 \text{ \AA} < \lambda \leq 6527 \text{ \AA}$, $6867 \text{ \AA} < \lambda < 6867.5 \text{ \AA}$, $6390 \text{ \AA} \leq \lambda < 7168 \text{ \AA}$, and $7312 \text{ \AA} \leq \lambda \leq 7419 \text{ \AA}$. $N_{\text{Sys,Red, NT}}$ refers to the number of systematics in non-telluric regions of the red arm and $N_{\text{Sys,Red, T}}$ refers to the number of systematics in telluric regions.

Species	$N_{\text{Sys,Red, NT}}$	$N_{\text{Sys,Red, T}}$	$N_{\text{Sys,Blue}}$	VMR
Na I	1	10	2	2.8×10^{-6}
Cr I	5	5	5	7.1×10^{-7}
Fe I	5	5	6	5.0×10^{-5}
Fe II	5	5	5	5.0×10^{-5}

fits and removes systematic effects, with the number of systematics to correct for N_{Sys} being the relevant input parameter. For the red arm, we run SYSREM on the telluric and non-telluric regions separately. We empirically determine the N_{Sys} that yields the greatest recovered SNR in each species as calculated with Equation 1. Optimal SYSREM iterations for the non-telluric regions of the red arm $N_{\text{Sys,Red, NT}}$, telluric regions of the red arm $N_{\text{Sys,Red, T}}$, and for the blue arm $N_{\text{Sys,Blue}}$ are given for each species in Table 3.

3.3. Cross-correlation

With data preparation complete, we cross-correlate model and observed spectra in the stellar rest frame, with the same procedure as described in M. C. Johnson et al. (2023). The cross-correlation procedure is adapted from the BANZAI-NRES package (C. McCully et al. 2022). Per-spectrum SNR is defined as

$$R_j(\phi) = P_{90} \left(\frac{f_j(\phi)}{\sigma_{f_j}(\phi)} \right) \quad (1)$$

where R_j is the P_{90} (90th percentile) of the ratio of residual flux $f_j(\phi)$ to error for the j^{th} spectrum and $\phi(t)$ is the planet orbital phase. The cross-correlation function is defined as

$$C(\phi, v) = \sum_{i=1}^{N_{\text{pixels}}} \frac{f_i(\phi) T_i(v)}{\sigma_{f_i}^2(\phi)} \quad (2)$$

where the index i is the pixel, $f_i(\phi)$ is residual flux at phase ϕ , $T_i(v)$ is the `petitRADTRANS` template spectrum Doppler-shifted to a radial velocity v , and $\sigma_{f_i}^2(\phi)$ is the variance of the residual flux. We compute CCF weights for the j^{th} spectrum with

$$w_j(\phi) = W R_j^2(\phi) \quad (3)$$

where W is the total equivalent width of the template spectrum of the species. The radial velocity of the planet as a function of time is

$$\text{RV}_p(\phi) = K_p \sin [2\pi\phi(t)] + v_{\text{sys}} + \Delta V(\phi) \quad (4)$$

where ΔV is the velocity offset of the lines or CCF being observed. We select a velocity range of $[-400, 400]$ km s^{-1} in 1 km s^{-1} steps. We stack each exposure's CCF with the weighted sum, then subtract off the median value M of the 2D map to correct for any offsets introduced by this process, yielding the full-transit CCF of single observation. We normalize the full-transit CCF amplitude with the standard deviation of the CCF σ_C at systemic velocity $|v_{\text{sys}}| > 100 \text{ km s}^{-1}$, yielding the SNR. We grid search for a SNR peak over planet radial velocity semi-amplitude $K_p \in [50, 350]$ km s^{-1} in steps of 1 km s^{-1} , yielding a $K_p - v_{\text{sys}}$ SNR map. For a point (K_p, v_{sys}) in the SNR map, this gives

$$\text{SNR}(K_p, v_{\text{sys}}) = \frac{1}{\sigma_C} \left[\sum_{j=1}^{N_{\text{spec}}} w_j(\phi) C(\phi, v) - M \right] \quad (5)$$

Next, we remove the Doppler shadow (described in more detail in Section 3.4). We use Equation 4 to calculate the planetary velocity at each exposure, assuming $\Delta V = 0$, then shift the full-transit CCFs into the planetary rest frame, i.e., we transform to $K_p - \Delta V$ space. Since e is consistent with zero, nominally $\Delta V = 0$ (M. B. Lund et al. 2017). Thus, a nonzero ΔV implies an atmospheric process is causing a line velocity offset; this value is also referred to as v_{wind} in some works.

We fit a Gaussian to the 1D CCF at K_p corresponding to the peak of the SNR map, i.e., peak K_p slice. We record the central radial velocity of the Gaussian fit in Table 4. We adapt the methods of A. Y. Kesseli et al. (2022) in calculating uncertainties of ΔV and K_p . That is, we divide the width of the fitted Gaussian by its SNR, then combine in quadrature with v_{sys} to yield the ΔV uncertainty. We also propagate error on the phase-resolved absorption traces to the full-transit CCFs, as discussed in Section 4.3.1. We calculate uncertainty on K_p by selecting upper and lower intervals that correspond to a 1σ decrease in SNR.

After completing the above process for each PEPSI arm separately, we coadd each arm into a CCF we henceforth refer to as the combined arm. We generate a combined arm $K_p - \Delta V$ SNR map via grid search and fit a Gaussian to the peak K_p slice.

3.4. Doppler shadow removal

As the planet crosses the stellar disk, the disk-integrated rotationally-broadened stellar absorption lines are deformed—a phenomenon known as the Rossiter-McLaughlin effect (RME; R. A. Rossiter 1924; D. B. McLaughlin 1924). A two dimensional effect of deformation in the CCF is the Doppler shadow. To correct for the RME, we employ a Doppler shadow model,

detailed in M. C. Johnson (2016) and further discussed in M. C. Johnson et al. (2014, 2017). In brief, we begin by dividing the stellar disk into surface elements defined by a 300×300 Cartesian grid, finding the fraction of each exposure time grid spaces are obscured or partially obscured by the planet. We scale the line profile contribution of each obscured surface element by this fraction, then convolve the line profiles with a Gaussian instrumental line profile. We assume solid body rotation and a Gaussian line profile in each surface element, scaled by quadratic limb darkening coefficients. We neglect macroturbulent broadening and gravity darkening (M. C. Johnson 2016). We subtract the out-of-transit line profile from the full line profile, revealing time-series CCF contribution of the transiting planet, known as the Doppler shadow. Using a normalized line profile, we fit to the Doppler shadow signature by limited non-linear least squares optimization with respect to spin-orbit alignment λ , impact parameter b , width of the Gaussian instrumental line profile, and a multiplicative scaling factor to transform the Doppler shadow into SNR space. Finally, we subtract the scaled Doppler shadow from the CCF. This process is demonstrated in Figure 3.

3.5. Detection criteria

We first examine `petitRADTRANS`-generated spectra, noting if the species has an abundance of lines in only one arm or both arms in the PEPSI CD III+V bandpass. Then, we examine the overlaid 1D CCFs, selecting whichever CCF has a peak $\text{SNR} \geq 3\sigma$, and selecting the combined CCF if both arms are individually $\geq 3\sigma$. We validate our detections by checking five criteria:

1. If there is $\geq 3\sigma$ SNR peak, it is a tentative detection, and if the SNR is $\geq 5\sigma$, it is a detection. Otherwise, we do not detect the species.
2. The CCF has a physically reasonable shape in $K_p - \Delta V$ space. A physically reasonable 2D CCF has $|\Delta V| \leq 15 \text{ km s}^{-1}$ and K_p consistent with $K_{p,\text{expected}}$, the planetary radial velocity semi-amplitude calculated from planetary parameters in Table 2.
3. There are no other CCF peaks on the map with an SNR within 1σ of the peak SNR that are within
 - (a) 1σ of K_p
 - (b) 25 km s^{-1} of ΔV .

See Appendix A.1 for examples.

4. If each arm of the spectrograph has a $\geq 3\sigma$ SNR peak, Gaussian fits to their line profiles must have

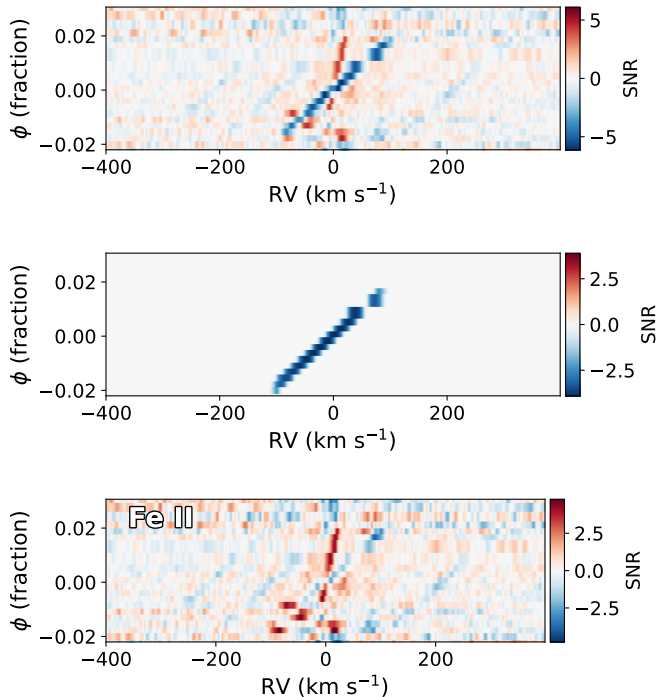


Figure 3. Removal of the Doppler shadow in the blue arm 2D CCF of Fe II. *Top:* 2D CCF of the blue arm Fe I signal for all N_{spec} exposures stacked. The Doppler Shadow (blue streak) intersects the atmospheric velocity signal (red streak near $RV = 0$, at the center of the Doppler shadow). *Middle:* Doppler shadow CCF generated by our model and fitted to our CCF data via non-linear least squares optimization. *Bottom:* Residual CCF after subtracting off the Doppler shadow.

centroids within $\pm 5 \text{ km s}^{-1}$ of each other. We show one example of detection and one example of nondetection in Appendix A.2 to further illustrate the criteria as they apply to template spectra and 1D CCFs. This condition could be generalized to other spectrographs that calculate CCFs spectra order-by-order by enforcing a consistent CCF velocity across the whole bandpass.

5. The detection is only valid if there is insignificant or no aliasing between the search species and strong lines from other species in the spectrum, as described in N. W. Borsato et al. (2023); S. Petz et al. (2023). In 1D CCFs, these artifacts manifest as peaks at both visually detectable nonphysical ΔV values, and as peaks overlapping with the absorption signal. In most cases, species with many lines, such as Fe I, interfere with species with few lines, such as Ba II, causing false atmospheric signals at otherwise reasonable velocity offsets. To correct for this, we first compute an aliased CCF

between the search species template and Fe I template, since Fe I is a strongly detected species with the most absorption lines in the PEPSI bandpass. We visually confirm that the aliased CCF peaks do not peak in the same location as the true CCF peak. We provide an example check in Appendix A.3. Future studies can fit the aliased CCF to the true CCF with a multiplicative scaling factor plus a constant offset in $K_p - \Delta V$ space, then subtract off, yielding the residual CCF. If the residual CCF remains unaltered in the immediate area of the 2D CCF and in the 1D line profile and Gaussian fit, they can verify the detection. If the residual CCF is altered, but the signal structure in $K_p - \Delta V$ space is consistent with the original CCF, they can report the detection characteristics of the original 2D full-transit CCF. They would discard the detection if the residual CCF is significantly altered.

3.6. Phase-resolved absorption signatures

We repeat the fitting procedure described in Section 3.3 but present each CCF in two distinct phase-binning schemes:

1. We divide the 1D CCF into a T_{1C} and T_{C4} bin at the $K_{p,\text{expected}}$ slice. We plot these along with the full-transit CCF to get the broadest view of any asymmetries. We use the same arm as the full-transit CCFs and fix $K_p = K_{p,\text{expected}}$. This is a common way to present phase-resolved CCFs, but it washes out the asymmetric signals from the limbs (A. B. Savel et al. 2023).
2. We confine each CCF function to an ingress bin (T_{12}), egress bin (T_{34}), three bins in T_{2C} , and three bins in T_{C3} . We use the same arm for phase-resolved CCFs as the full-transit CCF, but we do not apply the stringent detection criteria given in Section 3.5 to each bin. Instead, we fix $K_p = K_{p,\text{expected}}$ and fit a Gaussian to the SNR peak at $|\Delta V| \leq 15 \text{ km s}^{-1}$ in each bin. By dividing T_{23} into six bins, we seek to show the behavior of high SNR species during transit with a higher time resolution, more in line with theoretical models. We plot the CCF amplitude and ΔV as a function of phase, observing the change in line velocity between bins.

The results of each method are presented in Section 4.3.1.

4. RESULTS

4.1. Detections

To date, HRCCTS of KELT-20b has yielded detections of Fe I, Fe II, Na I, Ca II and tentative detections of Mg I, Cr II, and FeH (N. Casasayas-Barris et al. 2019; H. J. Hoeijmakers et al. 2020; S. K. Nugroho et al. 2020; M. Rainer et al. 2021; A. B. Langeveld et al. 2022; D. Sicilia et al. 2022). We confirm detections of Fe I and Fe II and tentative detections of Cr I and Na I (see Table 4 and Figure 4). The raw CCFs, 1D CCFs, 2D CCFs, and aliases with the Fe I template are shown for each detection and tentative detection in Appendix C.

Along with a majority of other observations, we detect Fe I and Fe II with high confidence. We find a blueshifted Fe I velocity offset $\Delta V_{\text{Fe I}} = -1.0 \pm 0.7 \text{ km s}^{-1}$. All studies that detected Fe I (M. Stangret et al. 2020; H. J. Hoeijmakers et al. 2020; S. K. Nugroho et al. 2020; M. Rainer et al. 2021) reported a greater blueshift than ours, ranging from -6.3 to -3.6 km s^{-1} .

We find the velocity of Fe II to be consistent with zero, which agrees with the CARMENES data of (S. K. Nugroho et al. 2020). Each of N. Casasayas-Barris et al. (2019); H. J. Hoeijmakers et al. (2020); A. Bello-Arufe et al. (2022); A. Pai Asnodkar et al. (2022) find a blueshifted Fe II velocity offset. S. K. Nugroho et al. (2020) reports a blueshifted Fe II velocity offset with the HARPS-N spectrograph. The S. K. Nugroho et al. (2020) observations, taken on different nights, suggest variability between observations and/or spectrographs, although the cause—whether physical, instrumental, or otherwise—remains unclear.

We tentatively detect redshifted $\Delta V_{\text{Na I}} = 2.5 \pm 1.3 \text{ km s}^{-1}$, which is inconsistent with all other Na I detections that reported blueshifts and were discrepant by $\sim 2 - 5 \text{ km s}^{-1}$ from our reported value (N. Casasayas-Barris et al. 2020; H. J. Hoeijmakers et al. 2020; S. K. Nugroho et al. 2020; A. B. Langeveld et al. 2022; D. Sicilia et al. 2022).

Cr I is a novel tentative detection that is significantly blueshifted $\Delta V_{\text{Cr I}} = -6.3 \pm 1.9 \text{ km s}^{-1}$.

Notably absent from our detections are Mg I, Ca I, and Ni I, each of which had an observability score ≥ 0.2 , as determined in Section 3.1. We do not detect ions Ca II and Cr II at $\geq 3\sigma$, which were detected in several other studies. Ca II’s lines fall outside of the PEPSI bandpass, unlike CARMENES (N. Casasayas-Barris et al. 2019; S. K. Nugroho et al. 2020) and HARPS-N (S. K. Nugroho et al. 2020). We also do not recover molecular species FeH, which was tentatively detected in a multi-planetary survey by A. Y. Kesseli et al. (2020).

4.2. Discrepancies between KELT-20b studies

Since KELT-20b has a longer orbital period and a lower orbital velocity relative to other UHJs, it is relatively insensitive to variations in mid-transit timing⁷. Thus, we do not attribute the discrepancy in velocity offsets observed across different KELT-20b studies to differences in the ephemerides used by each study, which is different from KELT-9b (A. Pai Asnodkar et al. 2022).

Since Fe I and Fe II are the strongest or nearly the strongest detections in most analyses of KELT-20b (M. Stangret et al. 2020; H. J. Hoeijmakers et al. 2020; S. K. Nugroho et al. 2020) and since the results of their relative velocity offsets in Figure 5 are largely inconsistent with one another, we propose that variation in data reduction methodologies are partially responsible for the discrepancies. Differences in self-consistent v_{sys} measurements or self-inconsistent v_{sys} assumptions may significantly impact reported full-transit velocity offsets and make studies of the same system difficult to reconcile. N. Casasayas-Barris et al. (2018); M. Stangret et al. (2020); H. J. Hoeijmakers et al. (2020); A. Y. Kesseli et al. (2020) each assume their v_{sys} from one of two discovery papers, M. B. Lund et al. (2017); G. J. J. Talens et al. (2018), rather than deriving their own from the stellar lines. $v_{\text{sys, Talens}}$ and $v_{\text{sys, Lund}}$ are discrepant by 2.2 km s^{-1} , or 5.6σ . Due to KELT-20’s rapid rotation⁸ and wide spectral lines, accurately measuring v_{sys} is difficult. Our v_{sys} is inconsistent with $v_{\text{sys, Talens}}$ by 15.0σ and inconsistent with $v_{\text{sys, Rainer}}$ by 7.4σ . The M. B. Lund et al. (2017) discovery paper and remaining measurements are $\leq 2\sigma$ discrepant with our v_{sys} (see Table 4).

We note a discrepancy between our Fe II full-transit CCF velocity offset and the reported SNR-weighted median Fe II velocity offset of four different datasets (including this one), computed by both line-by-line and cross-correlation spectroscopy of $\sim -2.0_{-0.7}^{+1.0} \text{ km s}^{-1}$ by A. Pai Asnodkar et al. (2022). They also report their full-transit CCF velocity offset of Fe II with only the PEPSI data (the same data used in this study) as $\sim -1.1 \pm 0.4 \text{ km s}^{-1}$ which is inconsistent by 1.6σ with our reported $\Delta V_{\text{Fe II}} = 0.0 \pm 0.5 \text{ km s}^{-1}$. Note that A. Pai Asnodkar et al. (2022) only used blue arm data, whereas we report the full-transit velocity offset of the telluric-corrected red and blue arms, combined. When

⁷ $\Delta(RV) \approx \frac{2\pi K_p \Delta T_0}{P}$, so a 10 minute offset in mid-transit time only yields a 2.1 km s^{-1} velocity difference, per the ephemerides listed in Table 2. In contrast, the given $\Delta T_0 = 1.64 \text{ s}$ only causes $\Delta(RV) \approx 5.8 \text{ m s}^{-1}$.

⁸ $v \sin I_* = 117.4 \pm 2.9 \text{ km s}^{-1}$, per M. B. Lund et al. (2017).

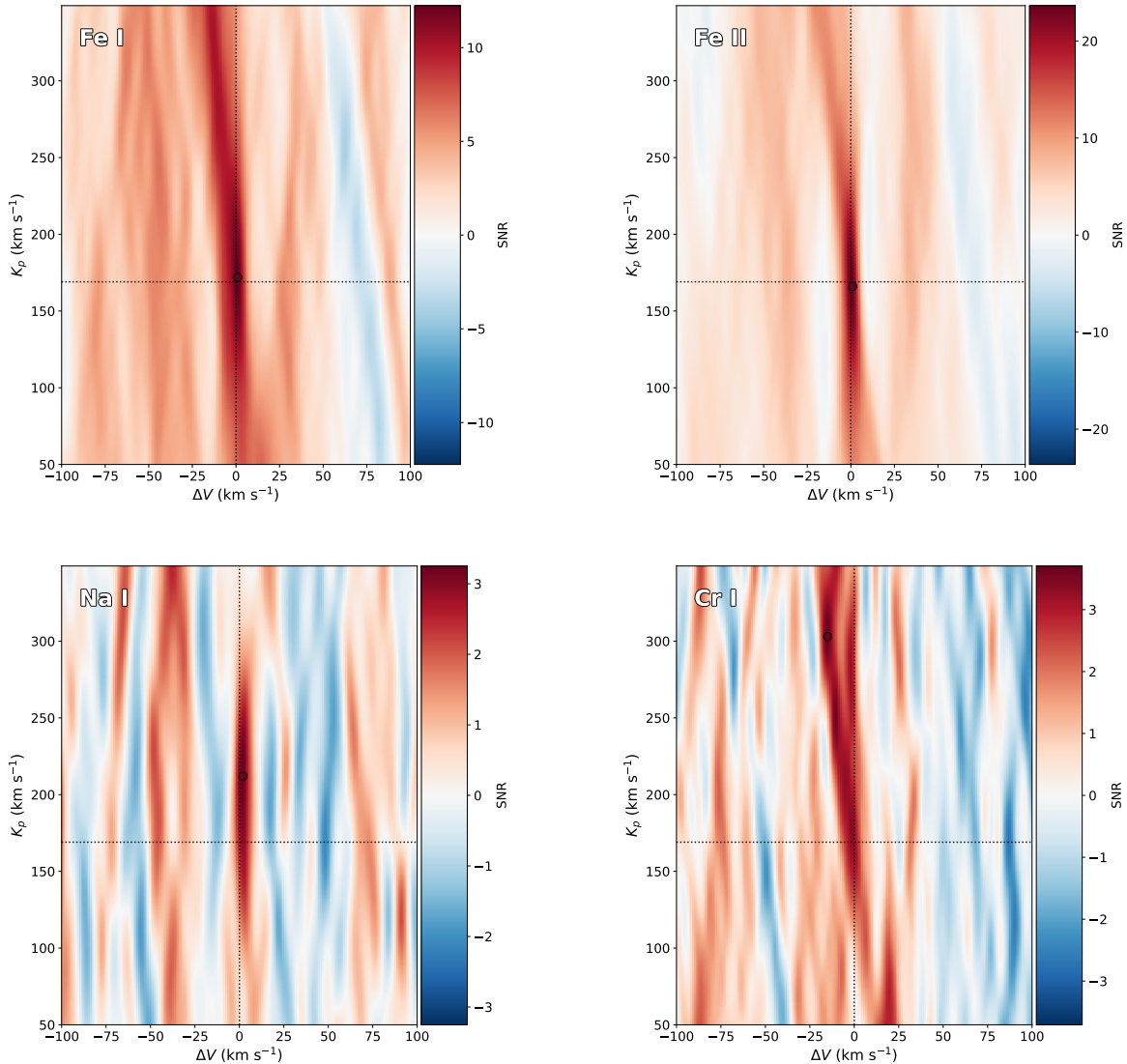


Figure 4. Combined arm 2D full-transit CCFs of species exceeding the tentative detection threshold. *Top left:* Fe I. *Top right:* Fe II. *Bottom left:* Na I. *Bottom right:* Cr I.

isolating our blue arm data, fixing $K_p = 177 \text{ km s}^{-19}$, and setting our systemic velocity equal to theirs, we recover a $-0.3 \pm 0.5 \text{ km s}^{-1}$ offset which is 1.2σ discrepant.

⁹ K_p of KELT-20b’s cross-correlation signal as measured by PEPSI and used for the Fe II cross-correlation analysis in A. Pai Asnodkar et al. (2022) but not presented in the paper (A. P. Asnodkar, personal correspondence, 2025 February 19). The K_p listed for A. Pai Asnodkar et al. (2022) in Table 4 was obtained from line-by-line Fe II analysis and was the KELT-20b K_p presented in that paper.

4.3. Dynamics

4.3.1. Confirming phase-dependence

To first ensure that the absorption traces vary with phase, we binned the first half T_{1C} and second half T_{C4} CCFs of Fe I and Fe II, selected the $K_{p,\text{expected}}$ slice, then plotted the 1D CCFs, as shown in Figure 6. Fe I exhibits clear blueshifting and confirms an asymmetrical absorption velocity prior to and post mid-transit. Fe II merely blueshifts by -1 km s^{-1} and thus does not demonstrate phase-dependence in the half-transit binning scheme.

Next, we compared a constant fit of the phase-binned CCFs to a linear fit. We empirically added a minimum error of $1/\sqrt{7} \text{ km s}^{-1}$ in quadrature to each point to

Table 4. Results of high-resolution line-by-line and cross-correlation transmission spectroscopy species detections in the atmosphere of KELT-20b. Note that ΔV is the full-transit averaged 1D CCF Gaussian velocity offset, so phase-resolved data is not present in this table. The source column letters correspond to the following papers: (a) N. Casasayas-Barris et al. (2019), (b) M. Stangret et al. (2020), (c) H. J. Hoeijmakers et al. (2020), (d) S. K. Nugroho et al. (2020), (e) A. Y. Kesseli et al. (2020), (f) M. Rainer et al. (2021), (g) A. B. Langeveld et al. (2022), (h) D. Sicilia et al. (2022), (i) A. Bello-Arufe et al. (2022), (j) A. Pai Asnodkar et al. (2022), (k) M. B. Lund et al. (2017), (m) G. J. J. Talens et al. (2018), (n) S. Petz et al. (2023).

Source	Spectrograph	N_{obs}	v_{sys} (km s ⁻¹)	Species	SNR (σ)	ΔV (km s ⁻¹)	FWHM (km s ⁻¹)	K_p (km s ⁻¹)
This work	PEPSI	1	$-22.78 \pm 0.11^{(n)}$	Na I	3.4	2.5 ± 1.3	8.7 ± 0.5	212^{+42}_{-59}
				Cr I	3.3	-6.3 ± 1.9	15.4 ± 1.8	252^{+2}_{-98}
				Fe I	11.9	-1.0 ± 0.7	15.8 ± 0.6	172^{+39}_{-4}
				Fe II	23.7	0.0 ± 0.5	9.8 ± 0.3	169^{+21}_{-1}
(a)	HARPS-N	3	$-21.07 \pm 0.03^{(m)}$	Na I	—	-3.1 ± 0.9	9.2 ± 2.0	176.6 ± 11.7
				Fe II	—	-2.8 ± 0.8	7.2 ± 1.2	174.4 ± 14.0
				H_{α}	—	-3.0 ± 1.2	19.0 ± 1.6	165.6 ± 16.7
				H_{β}	—	-1.2 ± 1.4	19.4 ± 2.5	136.2 ± 18.6
				H_{γ}	—	-2.3 ± 2.7	16.6 ± 4.2	135.0 ± 34.8
(b)	CARMENES	1	$-21.07 \pm 0.03^{(m)}$	Na I	—	-3.2 ± 1.7	8.0 ± 1.2	182.5 ± 14.3
				Ca II	—	-1.9 ± 0.6	9.2 ± 1.0	157.7 ± 8.2
				H_{α}	—	-4.5 ± 0.5	22.6 ± 0.9	166.2 ± 7.4
(c)	HARPS-N	3	$-21.07 \pm 0.03^{(m)}$	Fe I	10.5 ± 0.4	-6.3 ± 0.8	15.1 ± 0.6	121^{+86}_{-29}
				Fe II	8.6 ± 0.5	-2.8 ± 0.8	8.5 ± 0.6	155^{+18}_{-18}
(d)	EXPRES	1	$-23.30 \pm 0.40^{(k)}$	Mg I	3.33	-8.40 ± 1.40	33.45 ± 3.30	175
				Na I	3.40	-4.38 ± 0.54	10.07 ± 1.26	175
				Fe I	3.45	-4.81 ± 0.72	12.39 ± 1.69	175
				Fe II	4.60	-0.75 ± 0.37	8.54 ± 0.87	175
				Cr II	3.69	-3.40 ± 0.42	5.31 ± 0.99	175
(e)	HARPS-N	3	-22.06 ± 0.35	Na I	7.72	-1.4 ± 0.7	—	180.0 ± 11.8
				Fe I	14.30	-3.6 ± 0.3	—	200.1 ± 5.2
				Fe II	14.61	-1.4 ± 0.2	—	165.0 ± 3.5
				Ca II	7.53	2.2 ± 1.2	—	138.5 ± 15.3
	CARMENES	1	-22.02 ± 0.47	Na I	6.83	-0.6 ± 0.7	—	167.3 ± 12.1
				Fe I	6.44	-6.5 ± 0.6	—	263.1 ± 8.8
				Fe II	3.60	-0.4 ± 0.6	—	139.2 ± 2.5
				Ca II	8.60	0.1 ± 0.6	—	174.8 ± 8.2
(f)	CARMENES	1	$-23.3 \pm 0.3^{(k)}$	FeH	3.02	-0.5	—	158
(g)	HARPS-N	5	-24.48 ± 0.04	Fe I	—	$-4.7^{+0.3}_{-0.7}$	—	147^{+7}_{-6}
(h)	HARPS-N	3	—	Na I	—	-3.1 ± 1.9	—	—
(i)	HARPS-N	3	—	Na I D ₁	—	$-3.8^{+0.7}_{-0.7}$	$12.5^{+2.9}_{-2.3}$	$192.5^{+12.4}_{-13.5}$
				Na I D ₂	—	$-3.7^{+0.9}_{-0.9}$	$14.8^{+2.8}_{-2.4}$	$170.0^{+14.9}_{-13.5}$
				H_{α}	—	$-5.2^{+1.8}_{-1.7}$	$27.9^{+3.7}_{-3.3}$	$156.3^{+28.5}_{-27.0}$
(j)	FIES	2	-23.2 ± 0.4	Fe II	5.3	-20^{+6}_{-6}	—	120^{+78}_{-46}
(k)	(PEPSI, HARPS-N)	(1,3)	$-22.0978^{+0.4540}_{-0.4541}$	Fe II	—	$\sim -2.0^{+1.0}_{-0.7}$	—	$168.8^{+21.0}_{-12.4}$

reduce the goodness of fit of the stronger Fe II fit $\chi_{\nu}^2 \sim 1$. We found that for Fe II, the linear fit was statistically favored over the constant fit¹⁰. We also propagated the $1/\sqrt{7}$ km s⁻¹ error to the full-transit velocity offsets.

¹⁰ $\chi_{\nu, \text{linear}}^2 = 1.0$ and $\chi_{\nu, \text{constant}}^2 = 11.8$.

4.3.2. Features of Fe I and Fe II absorption traces

Fe I and Fe II exhibit distinct phase-resolved absorption signatures, as can be seen in Figure 7. To quantify the difference between their velocity offsets, we calculate the reduced chi-squared statistic given by

$$\chi_{\nu}^2 = \frac{1}{\nu} \sum_{n=1}^{N_{\text{bins}}} \frac{(\Delta V_{\text{Fe II}, n} - \Delta V_{\text{Fe I}, n})^2}{\sigma_{\Delta V_{\text{Fe II}, n}}^2 + \sigma_{\Delta V_{\text{Fe I}, n}}^2} \quad (6)$$

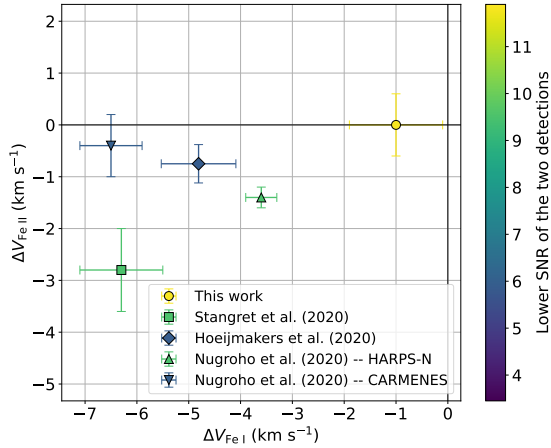


Figure 5. Scatter plot of the Fe I and Fe II full-transit binned velocity offsets in studies that detect both species. We find the lowest wind speeds for each species, but the blueshift of Fe I relative to Fe II is somewhat preserved: Fe I is blueshifted relative to Fe II by $\sim -1 \text{ km s}^{-1}$, which is inconsistent with other studies. Fe II is consistent with zero, in agreement with CARMENES observations by S. K. Nugroho et al. (2020). Our findings are inconsistent with the remaining studies of KELT-20b which detected both Fe I and Fe II.

where $\nu = N_{\text{bins}} = 8$. We obtain $\chi_{\nu}^2 = 20.1$, suggesting Fe I and Fe II are indeed probing distinct atmospheric regimes.

Fe I’s velocity is consistent with zero at ingress, redshifts somewhat up until T_C , then blueshifts. The largest blueshift is in the bin immediately following mid-transit, which then decreases and settles at a -2 km s^{-1} blueshift by egress. Fe I’s signal is weaker than Fe II’s in each phase bin, but both signals grow stronger with phase. Fe I’s signal is strongest at egress, where it exceeds 5σ .

Fe II is significantly redshifted at ingress, then steadily blueshifts from mid-transit to egress where it reaches a blueshift of -5 km s^{-1} . Fe II’s signal at the limbs is asymmetric in both signal strength and velocity. Egress SNR is $\sim 7\sigma$ greater than ingress SNR, and the egress signal is blueshifted -14 km s^{-1} relative to ingress. The Fe II signal is stronger than Fe I’s at all phases, so it is considered the best phase-resolved trace of the atmospheric absorption signal available in this work.

4.3.3. Comparison with previous phase-resolved studies

Our results are largely inconsistent with other KELT-20b observations with phase-resolved results. The Fe and Fe II velocity offsets are asymmetric between first half and second half of transit, unlike those in H. J. Hoeijmakers et al. (2020). However, each of our Fe I

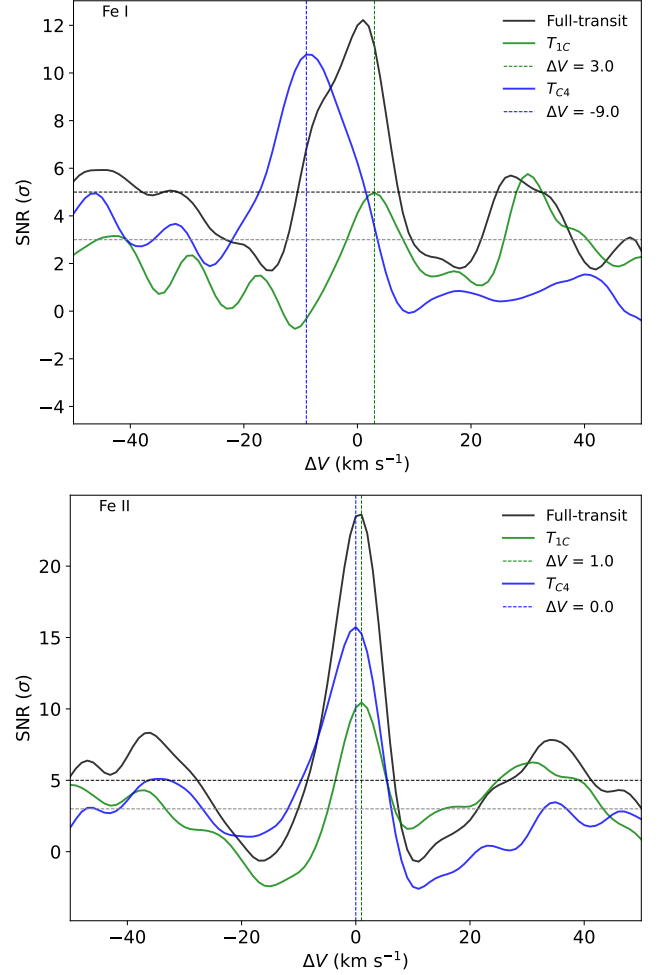


Figure 6. *Top:* Coadded Fe I 1D CCFs from T_{1C} in green, T_{C4} in blue, and full-transit in black. The gray horizontal dashed line is the tentative detection threshold and the black horizontal dashed line is the detection threshold. Center of a Gaussian fit to the T_{1C} and T_{C4} 1D CCFs are displayed in the legend. *Bottom:* The same plot for Fe II.

and Fe II phase binned signal strengths increase in the second half of transit, which is consistent with H. J. Hoeijmakers et al. (2020)’s findings.

M. Rainer et al. (2021)’s findings conflict with ours entirely. They observed five transits: three of five absorption traces do not exhibit a net Doppler shift, the other two redshift with phase. SNRs are consistent with each other in four of five transits, and one transit’s signal decreases in the second half. M. Rainer et al. (2021) also combines the five transits together and does not find a velocity shift or signal strength asymmetry. These discrepancies again motivate a more conclusive comparison to a KELT-20b-specific GCM and a continued observational campaign with rigorous detection methodology.

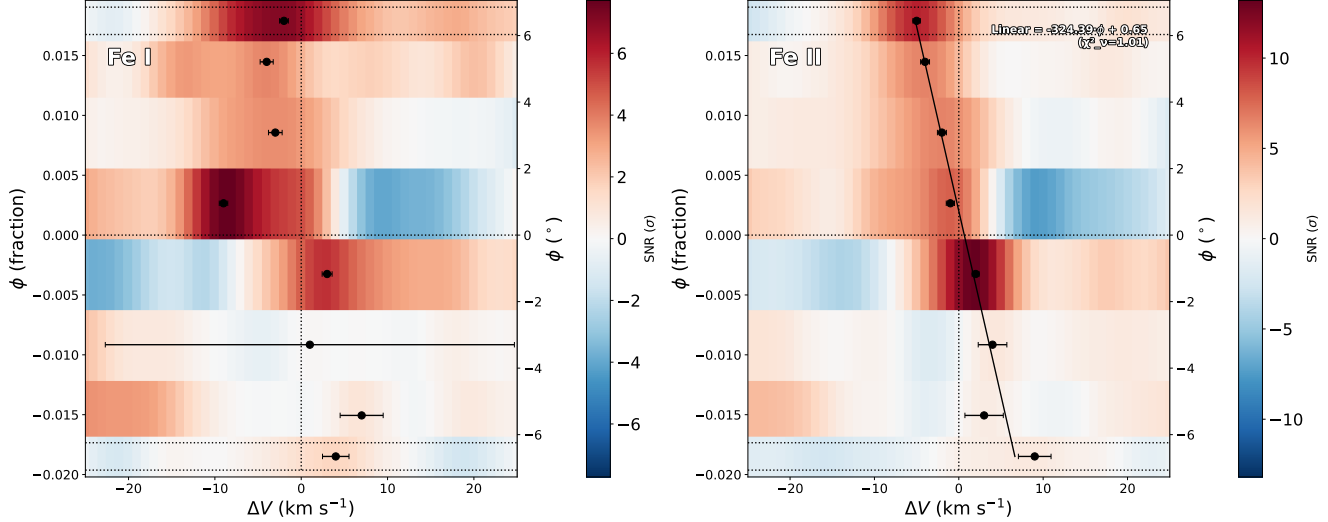


Figure 7. Phase-binned absorption traces of Fe I (left) and Fe II (right) with a linear fit. The parameters of the Fe II fit are shown in the top right. The horizontal dashed lines at the bottom delineate the ingress phase bin and those at the top delineate the egress phase bin.

4.3.4. Limb asymmetry and potential driving mechanisms

At egress, both Fe I and Fe II are blueshifted relative to ingress, which indicates day-to-nightside winds are present. We assume that as the hotter trailing limb rotates into view at egress, the transmission spectra probes a hotter region than at ingress. Thus, species with ions that have sufficient absorption within the PEPSI bandpass that are mostly unionized in the leading limb are expected to increase in signal strength as the trailing limb comes into view. Using the T. Guillot (2010) P-T profile from M. C. Johnson et al. (2023) in `petitRADTRANS`, we collect the temperatures corresponding to 10^{-3} bar and 10^{-6} bar, as well as T_{eq} from M. B. Lund et al. (2017). Using `FastChem`, we calculate the ionization fraction to connect the relative signal strength of each species during transit to the range of temperature regions probed by the spectra. As mentioned in Section 3.1, the P-T profile is unlikely to be particularly accurate, but we can rudimentarily constrain the regimes probed at ingress and egress.

By $T(10^{-6} \text{ bar}) = 4300 \text{ K}$, Fe is completely ionized, as seen in Figure 8. However, Fe I’s peak SNR is at egress, suggesting the temperature at trailing limb is lower than $T(10^{-6} \text{ bar})$. We again note that Fe II’s signal is stronger at egress than ingress as well, yet it still exceeds an SNR of 3σ in the ingress bin, suggesting a lower limit of $T = 3000 \text{ K}$ at the ingress limb. Note that we used a simplified P-T profile that assumes isothermal structure from the quench point until the thermal inversion, where it is linear in log space, then isothermal up to $T(10^{-6} \text{ bar})$ (M. C. Johnson et al. 2023). Nevertheless, this limb asymmetry suggests an interplay of asym-

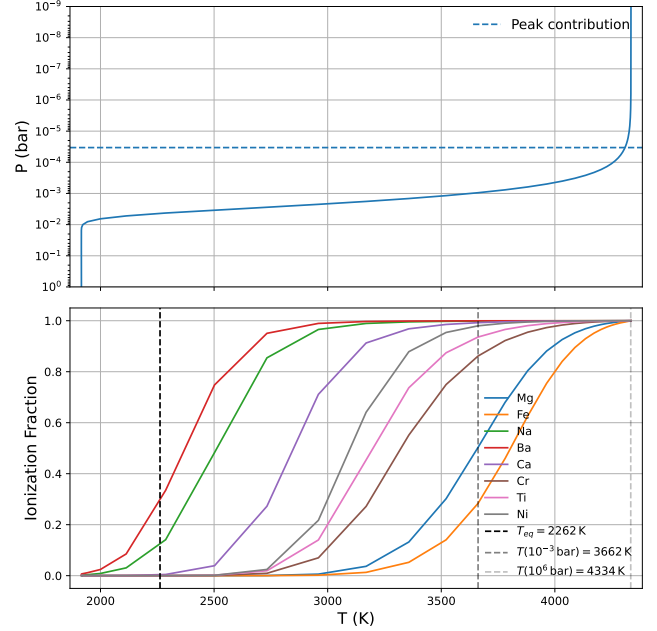


Figure 8. *Top:* P-T profile used in this work. *Bottom:* Ionization fraction for the atoms deemed detectable. We are using M. Asplund et al. (2021) extended solar abundances. Vertical lines correspond to T_{eq} , temperature in the P-T profile at 10^{-3} bar and temperature at 10^{-6} bar, in ascending order. The horizontal dashed line shows the estimated pressure at which the transmission contribution function peaks.

metry drivers, including increased scale height (further discussed in Section 4.3.5).

More broadly, our absorption signature is qualitatively similar to WASP-76b’s in that it blueshifts with phase and that signal strength increases in phase bins after mid-transit (D. Ehrenreich et al. 2020)—future model-

ing will be needed to pare down the potential drivers. A Ba II detection can also rudimentarily constrain the magnetic field strength when compared to a strong neutral species detection such as Fe I (A. B. Savel et al. 2024). Although we assessed Ba’s observability to be marginally above zero in Section 3.1, for Ba II we obtain a 2.9σ peak in the $K_p - \Delta V$ map at -6.4 km s^{-1} , as seen in Appendix A.3. However, there are several peaks of similar SNR across the map which violates our detection criteria, so we do not discuss this signal any further.

4.3.5. Comparison with theory

In both Fe I and Fe II, the net redshift extends past the ingress bin. The absorption trace does not cross over to a net blueshift until after mid-transit in both species (See Figure 7). The Fe I absorption trace also jumps after mid-transit to a blueshift, followed by a “bottoming out” of the signal, similar to the D. Ehrenreich et al. (2020) WASP-76b trace. This behavior is consistent with the absorption signature of the H. Beltz et al. (2023) active drag GCM, which includes a 3 G dipolar magnetic field aligned with the polar axis on WASP-76b. This detail is not present in the drag-free and uniform drag GCMs, making it a unique trait of the more computationally complex 3 G active drag treatment of magnetic effects that localizes the magnetic drag timescale to regions of the atmosphere. A model of KELT-20b that includes kinematic magnetohydrodynamics could test for this feature.

We also produce similar results to A. Simonnin et al. (2024)’s GCM for TOI-1518b which incorporates drag, albeit uniform. Fe II is assumed to be probed at a lower pressure than Fe I, and in A. Simonnin et al. (2024)’s strong drag model, wind speeds decrease in the upper atmosphere. This causes a continuous atmospheric trace of Fe II in the T_{23} region, whereas the Fe I trace jumps to a blueshift after T_C . This result is consistent with our own, as can be seen in Figure 7. This again suggests magnetic drag effects are visible in our results, but it does require theoretical corroboration.

Distinct behavior between Fe I and Fe II suggests we are probing multidimensional wind structures. Fe II is most likely probed at a lower pressure region than Fe I since it has greater speed at ingress and egress and a stronger signal.

A. B. Savel et al. (2023) models a 2200 K UHJ atmosphere and differentiates the impact of the scale height effect and thermal ionization on abundance asymmetries between leading and trailing limbs. Notably, A. B. Savel et al. (2023) finds that when isolating thermal ionization, most neutral species abundances are slightly

greater in the leading limb. This behavior is consistent with a decrease in neutral abundances due to thermal ionization, as discussed in Section 4.3.4. In A. B. Savel et al. (2023)’s model, the scale height effect is dominant, forcing nearly all species’ signals to be stronger in the trailing limb. In Figure 7, Fe I has a considerably stronger signal in the latter half of transit, suggesting that the scale height effect is the dominant asymmetry driver in our observation. However, the S/N levels of the spectra, as shown in Figure 1, are significantly higher in the second half of transit, which may also cause apparent signal strength differences. The S/N increase cannot exclusively be responsible for the signal strength asymmetry, given that the S/N increases $\sim 20\%$ while the detection significance increases $\sim 250\%$.

5. CONCLUSIONS

This paper presented an analysis of the high-resolution cross-correlation transmission spectrum of KELT-20b using an observation obtained with the PEPSI spectrograph. KELT-20b has been studied extensively with transmission spectroscopy and cross-correlation transmission spectroscopy, revealing an abundance of absorbers. This study confirmed 4 prior detections and presented 1 new tentative detection from an inventory of 58 species.

We recovered net blueshifts in 3 of 5 full-transit CCFs, supporting day-to-nightside winds proposed in several previous studies of KELT-20b. We present the detection results of all other works on this system, and find that full-transit velocity offset of the two strongest detections, Fe I and Fe II, are inconsistent with the majority of other studies. We presented stringent detection methodology to promote reproducibility and consistency in future HRCCTS studies and quantified discrepancies between systemic velocities of the discovery papers and observational works. We also assessed the observability of nondetections.

We phase-resolved the CCFs into ingress, egress, and six intermediate bins, revealing limb asymmetries in Fe I and Fe II. We found that the SNR increases from T_C to T_4 . We found similarity between our absorption traces and those post-processed from H. Beltz et al. (2023); A. Simonnin et al. (2024) GCMs that incorporate atmospheric drag. We also showed that a simple linear blueshift with phase is a stronger fit to the Fe II absorption trace than a constant offset. Again, our results are largely inconsistent with the two other studies that presented phase-resolved traces for KELT-20b.

Our phase-resolved results are broadly consistent with several dynamical mechanisms driving limb asymmetries, which motivates a theoretical treatment of KELT-

20b with non-ideal magnetohydrodynamics that is post-processed into phase-resolved absorption traces for comparison with this dataset and future observations. Likewise, our findings motivate an observational campaign of KELT-20b which combines time-series spectra from several high resolution spectrographs across different wavelength ranges. With meticulous detection methodology imposed, a benchmark set of observations would resolve inconsistencies with previous studies and unite observation with theory.

ACKNOWLEDGMENTS

CL thanks MCJ and the Summer Undergraduate Research Program in Astrophysics at The Ohio State University’s Department of Astronomy and Center for Cosmology and Astroparticle Physics for the opportunity to take on this project.

CL and MCJ are supported by NASA Grant 80NSSC23K0692.

The LBT is an international collaboration among institutions in the United States, Italy and Germany. LBT Corporation Members are: The Ohio State University, representing OSU, University of Notre Dame, University of Minnesota and University of Virginia; LBT Beteiligungsgesellschaft, Germany, representing the Max-Planck Society, The Leibniz Institute for Astrophysics Potsdam, and Heidelberg University; The University of Arizona on behalf of the Arizona Board of Regents; and the Istituto Nazionale di Astrofisica, Italy. Observations have benefited from the use of ALTA Center (alta.arcetri.inaf.it) forecasts performed with the Astro-Meso-Nh model. Initialization data of the ALTA automatic forecast system come from the General Circulation Model (HRES) of the European Centre for Medium Range Weather Forecasts.

The PEPSI spectra used in this paper will be made publicly available through the NASA Exoplanet Archive¹¹.

AUTHOR CONTRIBUTIONS

CL contributed to conceptualization, data curation, formal analysis, methodology, software development, visualization, writing the original draft, and reviewing and editing the manuscript.

MCJ contributed to conceptualization, data curation, formal analysis, funding acquisition, investigation, methodology, software development, supervision, and reviewing the manuscript.

JW contributed to conceptualization, funding acquisition, methodology, supervision, and reviewing the manuscript.

APA contributed to software development and reviewing the manuscript.

SP contributed to methodology, software development, and reviewing the manuscript.

AD contributed to investigation.

KGS contributed to data curation, resources, and reviewing the manuscript.

II contributed to data curation and resources.

Facilities: LBT(PEPSI)

Software: astropy (Astropy Collaboration et al. 2013), Jupyter (T. Kluyver et al. 2016), matplotlib (J. D. Hunter 2007), molecfit (W. Kausch et al. 2015; A. Smette et al. 2015), numpy (C. R. Harris et al. 2020), petitRADTRANS (P. Mollière et al. 2019), PyFastChem (J. W. Stock et al. 2018b), uncertainties E. O. LEBIGOT (2023)

¹¹ <https://exoplanetarchive.ipac.caltech.edu/docs/PEPSIMission.html>

APPENDIX

A. DETECTION CRITERIA EXAMPLES

A.1. Example 2D CCF check

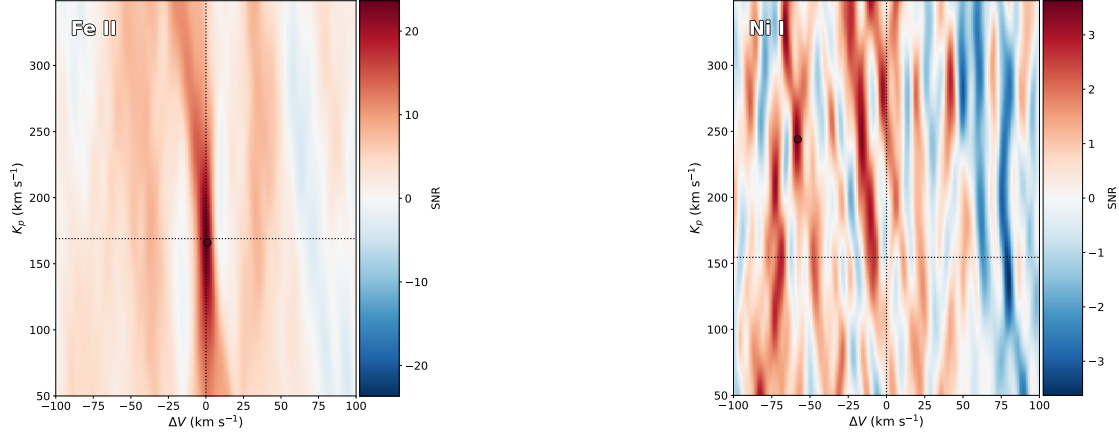


Figure 9. *Left:* Example of a physical atmospheric signature within an Fe II 2D CCF shifted into the planetary rest frame, or $K_p - \Delta V$ space. *Right:* Example of a likely nonphysical 2D CCF map of Ni I. Note the peak signal occurs at a nonphysical ΔV and K_p . Additionally, there are peaks throughout the map of a similar amplitude, indicating we are looking at noise. We do not consider this a detection.

A.2. Example template spectra and 1D CCF check

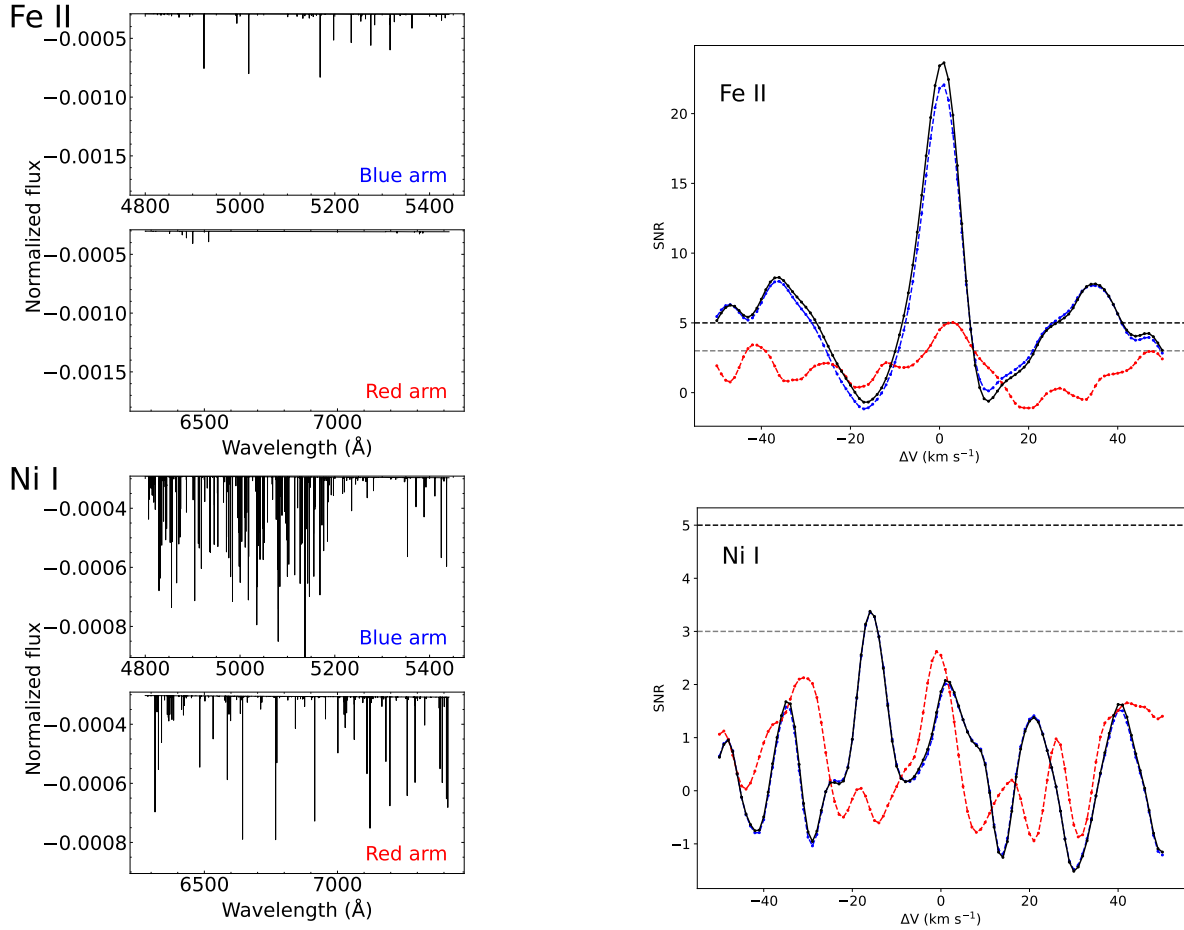


Figure 10. *Top:* On the left is the `petitRADTRANS`-generated transmission spectrum of Fe II, where we observe many deep lines in the blue arm, and few, weak lines in the red arm. On the right, the blue arm, red arm, and combined arm 1D CCFs are overlaid. The red arm 1D CCF is the red line, the blue arm 1D CCF is the blue line, and the combined arm 1D CCF is the black line. The gray dashed line is the tentative detection threshold and the black dashed line is the detection threshold. We observe a $\geq 5\sigma$ signal from each arm, and both have a peak within ± 5 km s⁻¹. Thus, we fit a Gaussian to the combined arm 1D CCF, as described in Section 3.6. *Bottom:* The same plots for Ni I where we see an abundance of lines in both arms. Upon inspection of the 1D CCF of each arm, there are peaks in the blue and red arm that are > 10 km s⁻¹. Since these low-confidence signals do not agree, we discard this detection. The same methodology is followed for the remainder of detected species, found in Table 2.

A.3. Example alias check

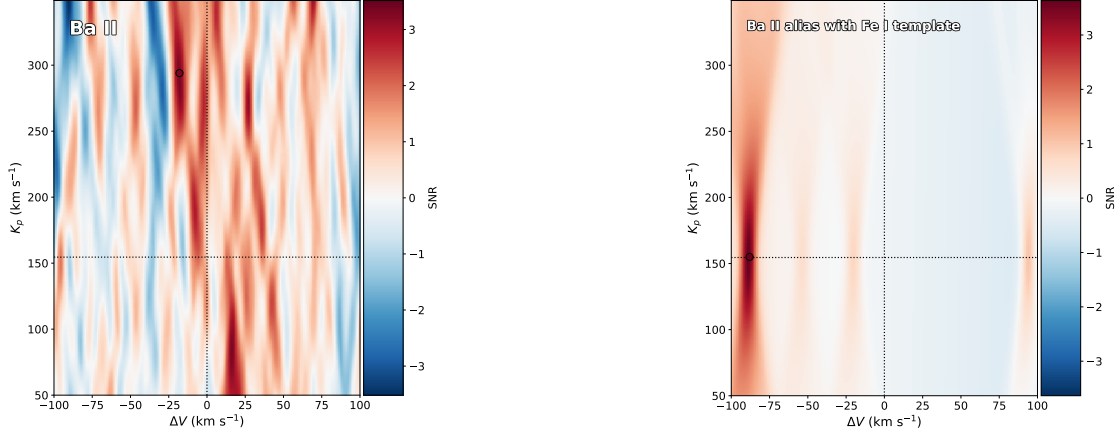


Figure 11. Example of a search species alias with the Fe I template, in this case of Ba II. *Left:* Ba II 2D CCF shifted into the planetary rest frame. *Right:* Alias between Fe I template and Ba II.

B. EQUATIONS

B.1. Observability score

Observability scores for each species were calculated using a modified version of the methodology from A. Y. Kesseli et al. (2022). The observability score S_k for species k is determined by the following equation:

$$S_k = \frac{1}{\max(S)} \left[\int_{\lambda_{\min, \text{red}}}^{\lambda_{\max, \text{red}}} \log \left(\frac{f_{\text{all}}(\lambda)}{f_k(\lambda)} \right) d\lambda + \int_{\lambda_{\min, \text{blue}}}^{\lambda_{\max, \text{blue}}} \log \left(\frac{f_{\text{all}}(\lambda)}{f_k(\lambda)} \right) d\lambda \right] \quad (\text{B1})$$

Here, $\lambda_{\min, \text{red}}$ and $\lambda_{\max, \text{red}}$ are the minimum and maximum wavelengths for the PEPSI red arm, respectively, and $\lambda_{\min, \text{blue}}$ and $\lambda_{\max, \text{blue}}$ correspond to the same for the blue arm. We also mask out the telluric regions on the red arm, but this is omitted from Equation B1 for brevity. f_{all} is the total flux across all species, while f_i is the flux excluding the species of interest. $\max(S)$ refers to the maximum value of the unnormalized scores. We transform the flux ratios to log space since they span several orders of magnitude. To compute flux ratios, we first generate a `petitRADTRANS` spectrum that includes the opacities of all species we considered in this study, as well as collision-induced continuum absorption opacities H₂-H₂ and H₂-He. We also consider H- bound-free and free-free absorption. Then, we generate the same spectrum minus the contribution of the search species k .

B.2. Doppler smearing

Doppler smearing occurs when the planetary velocity signal changes by more than one resolution element during an exposure (J. P. Wardenier et al. 2024; L. Boldt-Christmas et al. 2024). At mid-transit, the maximum exposure time for PEPSI observation of KELT-20b that avoids smearing is $\Delta t \sim \frac{cP}{2\pi\mathcal{R}K_p} \sim 650$ s, where c is the speed of light, P is the period of the planet, \mathcal{R} is the resolving power of the spectrograph, and K_p is the planetary radial velocity semi-amplitude.

C. DETECTION PROFILES

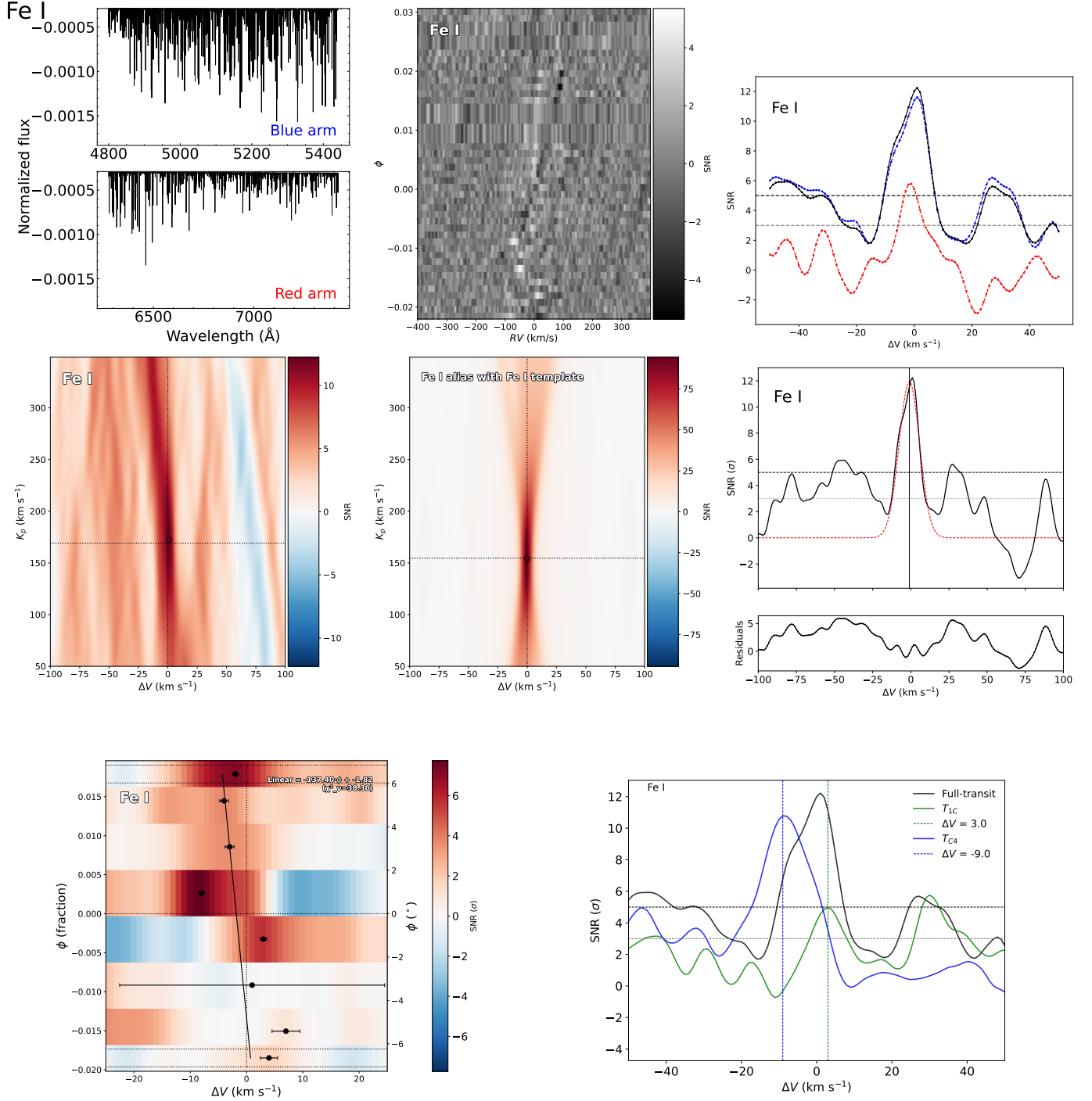


Figure 12. Detection profile for Fe I. *First row, left:* petitRADTRANS-generated transmission spectrum of Fe I containing many lines across the bandpass of both arms. *First row, middle:* 2D CCF with Doppler shadow correction applied, shifted into stellar rest frame. *First row, right:* Blue arm, red arm, and combined arm 1D CCFs overlaid. The red arm 1D CCF is the red line, the blue arm 1D CCF is the blue line, and the combined arm 1D CCF is the black line. The gray dashed line is the tentative detection threshold and the black dashed line is the detection threshold. We observe a $\geq 5\sigma$ signal from each arm, and both have a peak within $\pm 5 \text{ km s}^{-1}$. *Second row, left:* 2D $K_p - \Delta V$ map shifted into the planetary rest frame. *Second row, middle:* 2D CCF with alias between the species and Fe I template. Note that in this case, since we are searching for Fe I and aliasing with the Fe I template, the alias is an autocorrelation. *Second row, right:* 1D full-transit CCF at peak K_p . *Third row, left:* Phase-binned velocity offsets, i.e. centers of a Gaussian fit to the 1D CCF slice at $K_{p,\text{expected}}$ within each phase bin. The SNR is plotted to show the line strengths in each bin relative to each other. *Third row, right:* Coadded Fe I 1D CCFs from first half of transit in green, second half of transit in blue, and full-transit in black. The gray horizontal dashed line is the tentative detection threshold and the black horizontal dashed line is the detection threshold.

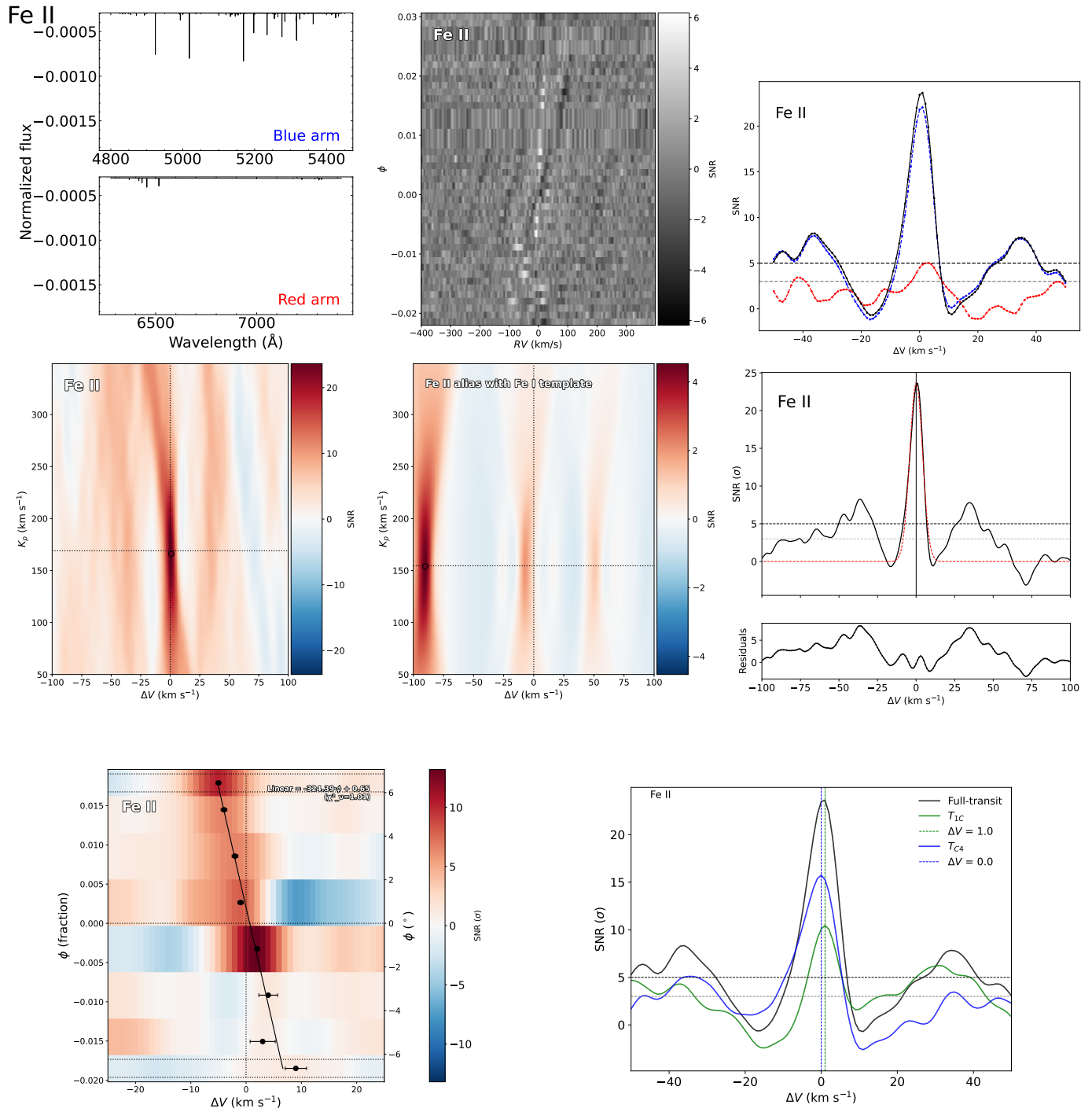


Figure 13. Same as Figure 12, but for Fe II.

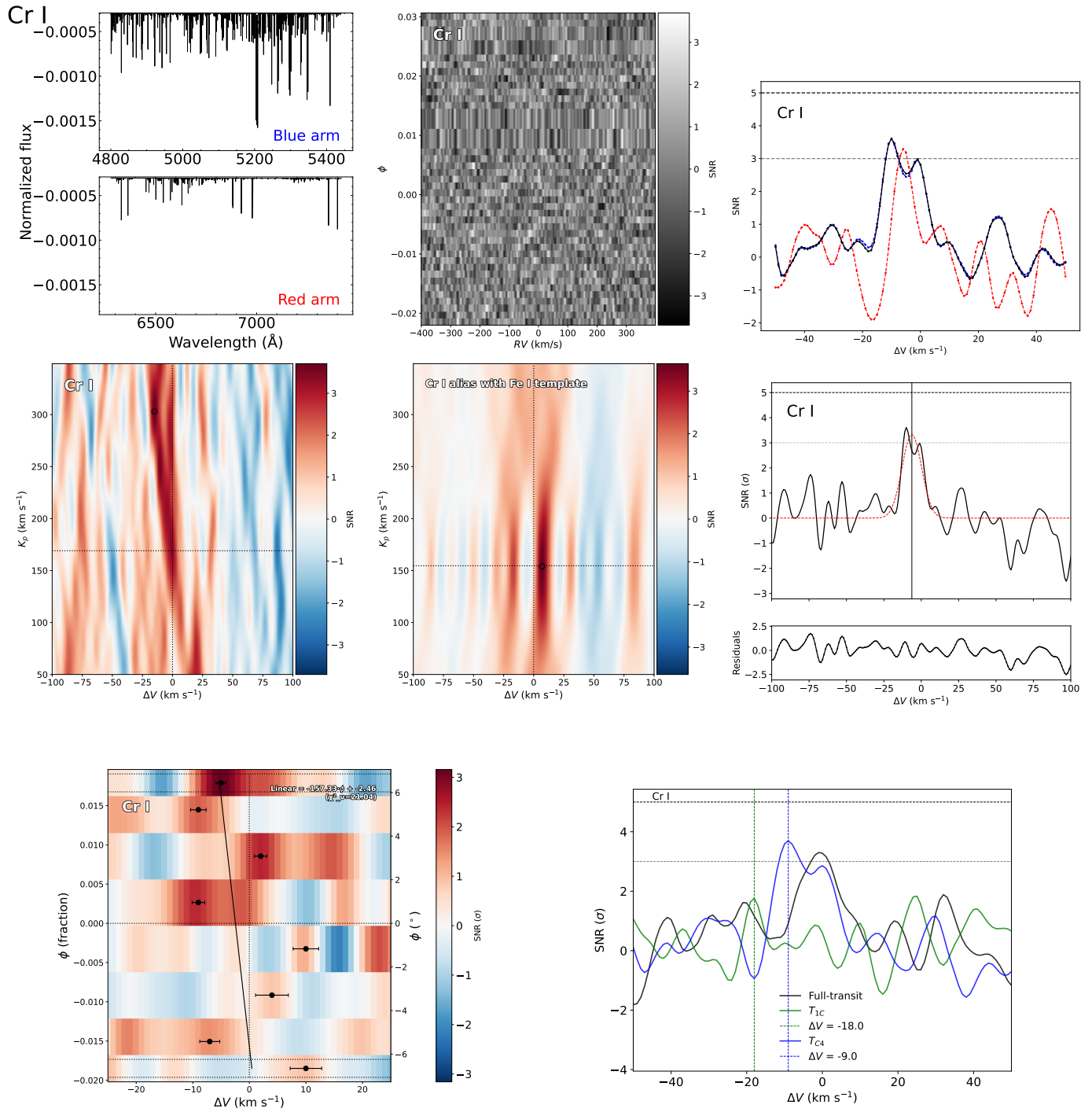


Figure 14. Same as Figure 12, but for Cr I.

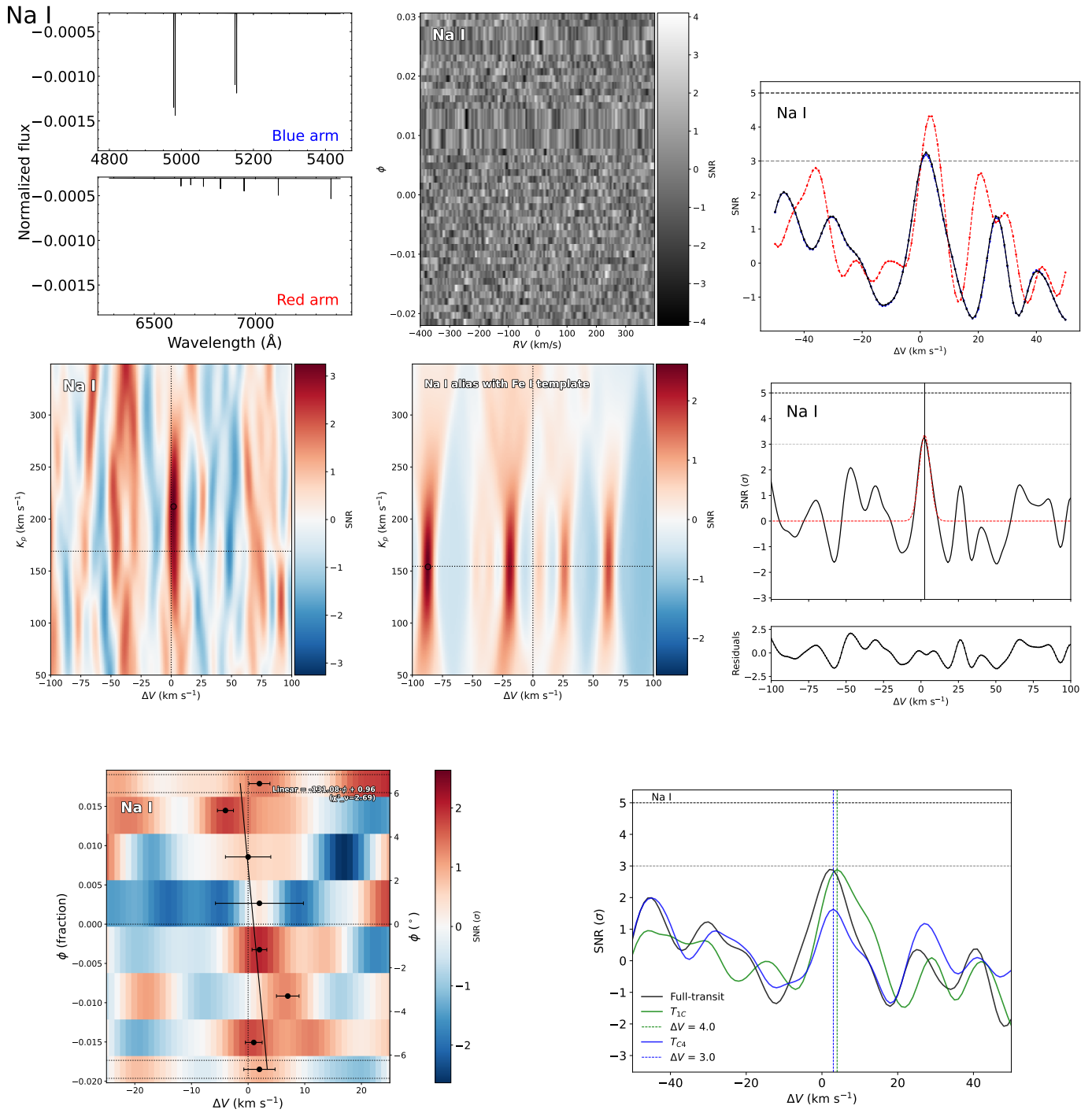


Figure 15. Same as Figure 12, but for Na I.

REFERENCES

- Asplund, M., Amarsi, A. M., & Grevesse, N. 2021, *A&A*, 653, A141, doi: [10.1051/0004-6361/202140445](https://doi.org/10.1051/0004-6361/202140445)
- Astropy Collaboration, Robitaille, T. P., Tollerud, E. J., et al. 2013, *A&A*, 558, A33, doi: [10.1051/0004-6361/201322068](https://doi.org/10.1051/0004-6361/201322068)
- Bello-Arufe, A., Buchhave, L. A., Mendonça, J. M., et al. 2022, *A&A*, 662, A51, doi: [10.1051/0004-6361/202142787](https://doi.org/10.1051/0004-6361/202142787)
- Beltz, H., Rauscher, E., Kempton, E. M.-R., et al. 2022, *AJ*, 164, 140, doi: [10.3847/1538-3881/ac897b](https://doi.org/10.3847/1538-3881/ac897b)
- Beltz, H., Rauscher, E., Kempton, E. M.-R., Malsky, I., & Savel, A. B. 2023, *AJ*, 165, 257, doi: [10.3847/1538-3881/acd24d](https://doi.org/10.3847/1538-3881/acd24d)
- Beltz, H., Rauscher, E., Roman, M. T., & Guilliatt, A. 2021, *AJ*, 163, 35, doi: [10.3847/1538-3881/ac3746](https://doi.org/10.3847/1538-3881/ac3746)
- Boldt-Christmas, L., Lesjak, F., Wehrhahn, A., et al. 2024, *A&A*, 683, A244, doi: [10.1051/0004-6361/202347398](https://doi.org/10.1051/0004-6361/202347398)
- Borsato, N. W., Hoeijmakers, H. J., Prinoth, B., et al. 2023, *A&A*, 673, A158, doi: [10.1051/0004-6361/202245121](https://doi.org/10.1051/0004-6361/202245121)
- Bowesman, C. A., Shuai, M., Yurchenko, S. N., & Tennyson, J. 2021, *MNRAS*, 508, 3181, doi: [10.1093/mnras/stab2525](https://doi.org/10.1093/mnras/stab2525)
- Casasayas-Barris, N., Pallé, E., Yan, F., et al. 2018, *A&A*, 616, A151, doi: [10.1051/0004-6361/201832963](https://doi.org/10.1051/0004-6361/201832963)
- Casasayas-Barris, N., Pallé, E., Yan, F., et al. 2019, *A&A*, 628, A9, doi: [10.1051/0004-6361/201935623](https://doi.org/10.1051/0004-6361/201935623)
- Casasayas-Barris, N., Pallé, E., Yan, F., et al. 2020, *A&A*, 640, C6, doi: [10.1051/0004-6361/201935623e](https://doi.org/10.1051/0004-6361/201935623e)
- Cauley, P. W., Shkolnik, E. L., Ilyin, I., et al. 2019, *AJ*, 157, 69, doi: [10.3847/1538-3881/aaf725](https://doi.org/10.3847/1538-3881/aaf725)
- Cauley, P. W., Wang, J., Shkolnik, E. L., et al. 2021, *AJ*, 161, 152, doi: [10.3847/1538-3881/abde43](https://doi.org/10.3847/1538-3881/abde43)
- Eastman, J. D., Rodriguez, J. E., Agol, E., et al. 2019, *arXiv*, doi: [10.48550/arxiv.1907.09480](https://doi.org/10.48550/arxiv.1907.09480)
- Ehrenreich, D., Lovis, C., Allart, R., et al. 2020, *Nature*, 580, 597601, doi: [10.1038/s41586-020-2107-1](https://doi.org/10.1038/s41586-020-2107-1)
- Guillot, T. 2010, *A&A*, 520, A27, doi: [10.1051/0004-6361/200913396](https://doi.org/10.1051/0004-6361/200913396)
- Harris, C. R., Millman, K. J., van der Walt, S. J., et al. 2020, *Nature*, 585, 357362, doi: [10.1038/s41586-020-2649-2](https://doi.org/10.1038/s41586-020-2649-2)
- Hoeijmakers, H. J., Cabot, S. H. C., Zhao, L., et al. 2020, *A&A*, 641, A120, doi: [10.1051/0004-6361/202037437](https://doi.org/10.1051/0004-6361/202037437)
- Hunter, J. D. 2007, *CiSE*, 9, 9095, doi: [10.1109/mcse.2007.55](https://doi.org/10.1109/mcse.2007.55)
- Ilyin, I. V. 2000, PhD thesis, University of Oulu, Finland
- Johnson, M. C. 2016, PhD thesis, The University of Texas at Austin
- Johnson, M. C., Cochran, W. D., Addison, B. C., Tinney, C. G., & Wright, D. J. 2017, *AJ*, 154, 137, doi: [10.3847/1538-3881/aa8462](https://doi.org/10.3847/1538-3881/aa8462)
- Johnson, M. C., Cochran, W. D., Albrecht, S., et al. 2014, *ApJ*, 790, 30, doi: [10.1088/0004-637x/790/1/30](https://doi.org/10.1088/0004-637x/790/1/30)
- Johnson, M. C., Wang, J., Asnodkar, A. P., et al. 2023, *AJ*, 165, 157, doi: [10.3847/1538-3881/acb7e2](https://doi.org/10.3847/1538-3881/acb7e2)
- Kausch, W., Noll, S., Smette, A., et al. 2015, *A&A*, 576, A78, doi: [10.1051/0004-6361/201423909](https://doi.org/10.1051/0004-6361/201423909)
- Kesseli, A. Y., Snellen, I. A. G., Alonso-Floriano, F. J., Mollière, P., & Serindag, D. B. 2020, *AJ*, 160, 228, doi: [10.3847/1538-3881/abb59c](https://doi.org/10.3847/1538-3881/abb59c)
- Kesseli, A. Y., Snellen, I. A. G., Casasayas-Barris, N., Mollière, P., & Sánchez-López, A. 2022, *AJ*, 163, 107, doi: [10.3847/1538-3881/ac4336](https://doi.org/10.3847/1538-3881/ac4336)
- Kitzmann, D., Stock, J. W., & Patzer, A. B. C. 2023, *MNRAS*, 527, 72637283, doi: [10.1093/mnras/stad3515](https://doi.org/10.1093/mnras/stad3515)
- Kluyver, T., Ragan-Kelley, B., Pérez, F., et al. 2016, in *Positioning and Power in Academic Publishing: Players, Agents and Agendas*, IOS Press, 87–90
- Langeveld, A. B., Madhusudhan, N., & Cabot, S. H. C. 2022, *MNRAS*, 514, 51925213, doi: [10.1093/mnras/stac1539](https://doi.org/10.1093/mnras/stac1539)
- LEBIGOT, E. O. 2023, <https://pythonhosted.org/uncertainties/>
- Lund, M. B., Rodriguez, J. E., Zhou, G., et al. 2017, *AJ*, 154, 194, doi: [10.3847/1538-3881/aa8f95](https://doi.org/10.3847/1538-3881/aa8f95)
- McCully, C., Daily, M., Brandt, G. M., et al. 2022, in *Software and Cyberinfrastructure for Astronomy VII*, ed. J. Ibsen & G. Chiozzi, Vol. 12189 (SPIE), 1218914, doi: [10.1117/12.2630667](https://doi.org/10.1117/12.2630667)
- McLaughlin, D. B. 1924, *ApJ*, 60, 22, doi: [10.1086/142826](https://doi.org/10.1086/142826)
- Miller-Ricci Kempton, E., & Rauscher, E. 2012, *ApJ*, 751, 117, doi: [10.1088/0004-637x/751/2/117](https://doi.org/10.1088/0004-637x/751/2/117)
- Mollière, P., Wardenier, J. P., van Boekel, R., et al. 2019, *A&A*, 627, A67, doi: [10.1051/0004-6361/201935470](https://doi.org/10.1051/0004-6361/201935470)
- Nugroho, S. K., Gibson, N. P., de Mooij, E. J. W., et al. 2020, *MNRAS*, 496, 504, doi: [10.1093/mnras/staa1459](https://doi.org/10.1093/mnras/staa1459)
- Pai Asnodkar, A., Wang, J., Eastman, J. D., et al. 2022, *Astron. J.*, 163, 155
- Petz, S., Johnson, M. C., Asnodkar, A. P., et al. 2023, *MNRAS*, 527, 70797092, doi: [10.1093/mnras/stad3481](https://doi.org/10.1093/mnras/stad3481)
- Pino, L., Brogi, M., Désert, J. M., et al. 2022, *A&A*, 668, A176, doi: [10.1051/0004-6361/202244593](https://doi.org/10.1051/0004-6361/202244593)
- Prinoth, B., Hoeijmakers, H. J., Pelletier, S., et al. 2023, *A&A*, 678, A182, doi: [10.1051/0004-6361/202347262](https://doi.org/10.1051/0004-6361/202347262)
- Rainer, M., Borsa, F., Pino, L., et al. 2021, *A&A*, 649, A29, doi: [10.1051/0004-6361/202039247](https://doi.org/10.1051/0004-6361/202039247)

- Rivlin, T., Lodi, L., Yurchenko, S. N., Tennyson, J., & Le Roy, R. J. 2015, *MNRAS*, 451, 634638, doi: [10.1093/mnras/stv979](https://doi.org/10.1093/mnras/stv979)
- Rossiter, R. A. 1924, *ApJ*, 60, 15, doi: [10.1086/142825](https://doi.org/10.1086/142825)
- Savel, A. B., Beltz, H., Komacek, T. D., Tsai, S.-M., & Kempton, E. M.-R. 2024, *ApJL*, 969, L27, doi: [10.3847/2041-8213/ad5a0a](https://doi.org/10.3847/2041-8213/ad5a0a)
- Savel, A. B., Kempton, E. M.-R., Rauscher, E., et al. 2023, *ApJ*, 944, 99, doi: [10.3847/1538-4357/acb141](https://doi.org/10.3847/1538-4357/acb141)
- Savel, A. B., Kempton, E. M.-R., Malik, M., et al. 2022, *ApJ*, 926, 85, doi: [10.3847/1538-4357/ac423f](https://doi.org/10.3847/1538-4357/ac423f)
- Sicilia, D., Malavolta, L., Pino, L., et al. 2022, *A&A*, 667, A19, doi: [10.1051/0004-6361/202244055](https://doi.org/10.1051/0004-6361/202244055)
- Simonnin, A., Parmentier, V., Wardenier, J. P., et al. 2024, arXiv, doi: [10.48550/ARXIV.2412.01472](https://doi.org/10.48550/ARXIV.2412.01472)
- Smette, A., Sana, H., Noll, S., et al. 2015, *A&A*, 576, A77, doi: [10.1051/0004-6361/201423932](https://doi.org/10.1051/0004-6361/201423932)
- Snellen, I. A. G., de Kok, R. J., de Mooij, E. J. W., & Albrecht, S. 2010, *Nature*, 465, 10491051, doi: [10.1038/nature09111](https://doi.org/10.1038/nature09111)
- Stangret, M., Casasayas-Barris, N., Pallé, E., et al. 2022, *A&A*, 662, A101, doi: [10.1051/0004-6361/202141799](https://doi.org/10.1051/0004-6361/202141799)
- Stangret, M., Casasayas-Barris, N., Pallé, E., et al. 2020, *A&A*, 638, A26, doi: [10.1051/0004-6361/202037541](https://doi.org/10.1051/0004-6361/202037541)
- Stock, J. W., Kitzmann, D., & Patzer, A. B. C. 2022, *MNRAS*, 517, 40704080, doi: [10.1093/mnras/stac2623](https://doi.org/10.1093/mnras/stac2623)
- Stock, J. W., Kitzmann, D., Patzer, A. B. C., & Sedlmayr, E. 2018a, *MNRAS*, doi: [10.1093/mnras/sty1531](https://doi.org/10.1093/mnras/sty1531)
- Stock, J. W., Kitzmann, D., Patzer, A. B. C., & Sedlmayr, E. 2018b, *MNRAS*, doi: [10.1093/mnras/sty1531](https://doi.org/10.1093/mnras/sty1531)
- Strassmeier, K., Ilyin, I., Järvinen, A., et al. 2015, *Astronomische Nachrichten*, 336, 324361, doi: [10.1002/asna.201512172](https://doi.org/10.1002/asna.201512172)
- Strassmeier, K. G., Ilyin, I., & Steffen, M. 2018, *A&A*, 612, A44, doi: [10.1051/0004-6361/201731631](https://doi.org/10.1051/0004-6361/201731631)
- Talens, G. J. J., Justesen, A. B., Albrecht, S., et al. 2018, *A&A*, 612, A57, doi: [10.1051/0004-6361/201731512](https://doi.org/10.1051/0004-6361/201731512)
- Tamuz, O., Mazeh, T., & Zucker, S. 2005, *MNRAS*, 356, 14661470, doi: [10.1111/j.1365-2966.2004.08585.x](https://doi.org/10.1111/j.1365-2966.2004.08585.x)
- Wardenier, J. P., Parmentier, V., Lee, E. K. H., Line, M. R., & Gharib-Nezhad, E. 2021, *MNRAS*, 506, 12581283, doi: [10.1093/mnras/stab1797](https://doi.org/10.1093/mnras/stab1797)
- Wardenier, J. P., Parmentier, V., Line, M. R., & Lee, E. K. H. 2023, *MNRAS*, 525, 49424961, doi: [10.1093/mnras/stad2586](https://doi.org/10.1093/mnras/stad2586)
- Wardenier, J. P., Parmentier, V., Line, M. R., et al. 2024, *PASP*, 136, 084403, doi: [10.1088/1538-3873/ad5c9f](https://doi.org/10.1088/1538-3873/ad5c9f)
- Yurchenko, S. N., Blissett, A., Asari, U., et al. 2016, *MNRAS*, 456, 45244532, doi: [10.1093/mnras/stv2858](https://doi.org/10.1093/mnras/stv2858)